Metallic Plasmonic Nanostructure Arrays for Enhanced Solar Photocatalysis

Huaping Jia[1,2,3], Chi Chung Tsoi[2,3], Abdel El Abed[4], Weixing Yu[5], Aoqun Jian[1*], Shengbo Sang[1*], and Xuming Zhang[2,3*]

[1]Shanxi Key Laboratory of Micro Nano Sensors & Artificial Intelligence Perception, College of Information, Taiyuan University of Technology, Taiyuan 030024, China

[2]Department of Applied Physics, The Hong Kong Polytechnic University, Kowloon, Hong Kong 999077, China

[3]Photonics Research Institute, The Hong Kong Polytechnic University, Hung Hom, Kowloon, Hong Kong 999077, China

[4]Laboratoire Lumière Matière et Interfaces (LuMIn), Institut d'Alembert, ENS Paris Saclay, CentraleSupélec, Université Paris-Saclay, 4 avenue des Sciences, 91190 Gif-sur-Yvette, France

[5]Key Laboratory of Spectral Imaging Technology, Xi'an Institute of Optics and Precision Mechanics, Chinese Academy of Sciences, Xi'an 710000, China

Abstract

Plasmon-enhanced photocatalysis has emerged as a promising technology for solar-to-chemical energy conversion. Compared to isolated or disordered metal nanostructures, by controlling the morphology, composition, size, spacing, and dispersion of individual nanocomponents, plasmonic nanostructure arrays with coupling architectures yield strong broadband light-harvesting capability, efficient charge transfer, enhanced local electromagnetic fields, and large contact interfaces. Although metallic nanostructure arrays have been extensively studied for various applications, such as refractive index sensing, surface-enhanced spectroscopy, plasmon-enhanced luminescence, plasmon nanolasing, and perfect light absorption, the connection between surface plasmon resonance (SPR) and enhanced photocatalysis remains relatively unexplored. In this study, we present an overview of plasmonic nanostructure arrays over a broad range, from zero-dimensional (0D) to three-dimensional (3D), for efficient photocatalysis. By reviewing the fundamental mechanisms, recent applications, and latest developments of plasmonic nanostructure arrays in solar-driven chemical conversion, this study reports on the latest guidance towards the integration of plasmonic nanostructures for functional devices in the fields of plasmonic, photonics, photodetection, and solar-energy harvesting.

Keywords

Plasmonic, nanostructure arrays, surface plasmon resonance, enhanced photocatalysis, solar energy conversion

1. Introduction

With the rapid development of the global economy, energy shortages and environmental pollution have emerged as considerable challenges for mankind. Solar energy is a globally

distributed energy source and is advantageous in term of its high regional universality, cleanliness, and sustainability. In recent decades, photocatalysis has materialized as a promising research approach for exploring the conversion of solar energy into chemical energy, such as hydrogen generation, organic pollutant degradation, and photosynthesis.[1–10] The photocatalytic performance of semiconductors relies heavily on two factors: light absorption and charge-carrier generation/separation/transport processes.[11,12] However, limited light absorption and rapid charge recombination are two common bottlenecks in this field.[13–16] In particular, semiconductors with wide bandgaps (>3 eV) such as TiO_2 can only absorb ultraviolet (UV) light; thus, the energy corresponding to the visible and infrared (IR) regions remain unutilized, which account for 42% and 54% of the solar energy, respectively.

Recently, plasmonic metal nanomaterials have been introduced into solar-energy conversion systems, such as photovoltaics (solar cells), phototherapy, and solar-driven reactions. Plasmonic nanostructures exhibit strong and unique optical responses and can interact with incident photons via surface plasmon resonance (SPR) excitation. This resonance process is beneficial for photocatalysis, such as efficient light-harvesting in the visible and near-infrared ranges, hot electron–hole pair generation, enhanced scattering, hot-electron injection (HEI), local electromagnetic-field enhancement (LEMF), plasmon-induced resonant energy transfer (PIRET), and photothermal heating effects.[17–27] In several studies, hot electrons were generated either via localized surface plasmon resonance (LSPR) in free-standing individual nanostructures, such as metal nanoparticles and nanorods),[17,28–32] or through surface plasmon polaritons (SPPs) in continuous patterned metal nanostructures.[33–37]

Among the various plasmonic nanostructures, arrays-structure have drawn great interest owing to their large surface-to-volume ratio, tunable nanoscale features, distinctive optical performance, high regularity, and high electrical conductivity. Their optical properties are mainly dependent on the size, shape, and periodicity of their structures.[8,36,38] Under resonance conditions, plasmons can efficiently couple light into nanostructures, confining it within the diffraction limit. In addition to the basic yet prominent SPR effects, such as LSPR and SPPs, plasmonic nanostructure arrays are advantageous for producing and tuning plasmonic modes such as extraordinary transmission, Fabry–Pérot (F–P) cavity mode, surface lattice resonance (SLR), plasmonic gap mode, and Fano resonance.[38–40] Moreover, owing to the ordered spatial arrangement of plasmonic nanostructure arrays, the processes of electrochemical reactions in each unit cell are optimally separated from the neighboring parts, thereby suppressing possible reverse processes.[41–43] Accordingly, plasmonic nanostructure arrays exhibit a superior performance in the conversion of solar energy into chemical energy, for example, in H_2 generation, photocatalysis, and photosynthesis.

To the best of our knowledge, the related prior review articles on metallic plasmonic arrays have primarily focused on applications such as refractive index sensors, surface-enhanced spectroscopy, plasmon-enhanced luminescence, nanoscale plasmon lasing, and energy storage devices.[38,40,44–47] Additionally, in the field of solar energy conversion, extensive reviews have generally reported on semiconductor nanostructure arrays or plasmon-mediated semiconductor

structures; however, metallic nanostructure arrays have remained largely unexplored.[18,48–54] Hence, a detailed discussion of the connection between the SPR effects of metallic nanostructure arrays and enhanced photocatalysis is still lacking in the literature. In this review, we characterized the enhanced photocatalytic performance of plasmonic nanostructure arrays for a broad range of structural designs aiming at formulating updated guidelines for solar energy conversion. First, we reviewed various light-management mechanisms and fabrication methods for nanostructure arrays. Plasmonic nanostructure arrays are categorized into zero-dimensional (0D) and three-dimensional (3D) structures (refer to Figure 1). Subsequently, we presented the working principles and relationship between plasmonic nanostructure arrays and solar-energy conversion performance. In particular, comprehensive studies have reported on key processes (e.g., LSPR, SPPs, and other coupled-resonance modes) that play major roles in solar energy capture and conversion. Moreover, we illustrated the perspectives of plasmonic nanostructure arrays for converting solar energy into chemical energy, such as water splitting, photocatalysis, and photodegradation. Finally, we identified future directions of plasmonic nanostructure arrays and drew conclusions based on our findings, as presented herein.

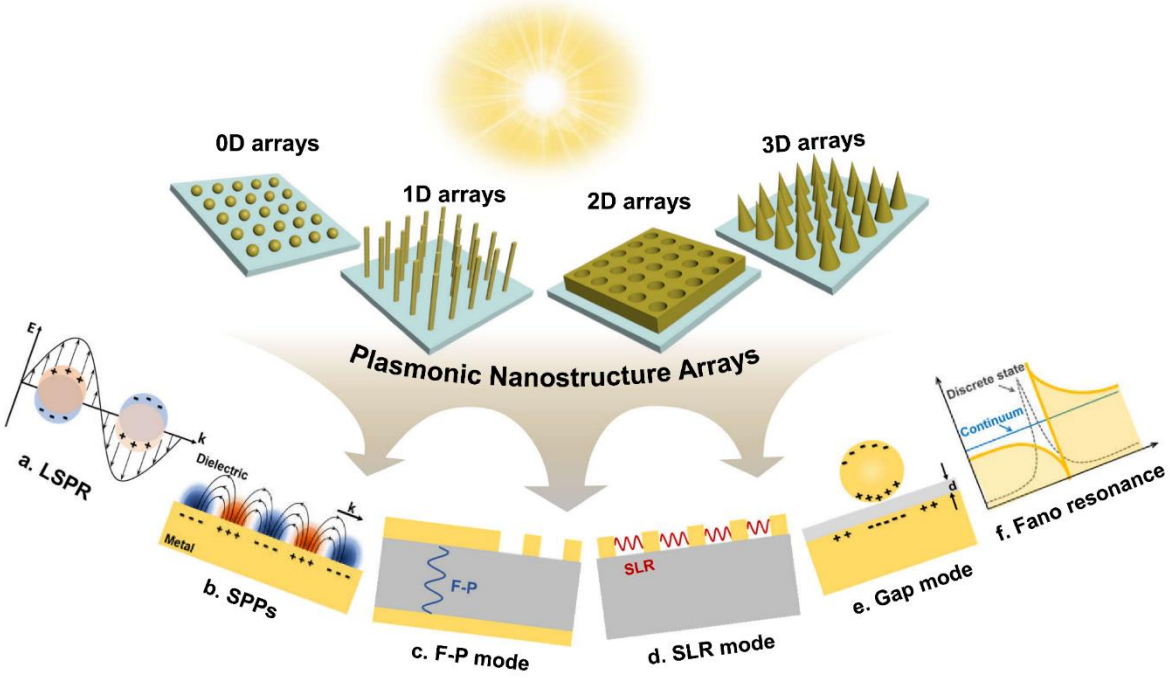

Figure 1. Classification of plasmonic nanostructure arrays as zero-dimensional (0D), one-dimensional (1D), two-dimensional (2D), and three-dimensional (3D) arrays. Various light-management mechanisms in nanostructure arrays: (a) localized surface plasmon resonance (LSPR) effect, (b) surface plasmon polaritons (SPPs) mode on the surface of plasmonic arrays, (c) Fabry–Pérot (F–P) cavity mode generated through metal–dielectric–metal three-layer structures, (d) surface lattice resonance (SLR) mode generated via ordered plasmonic arrays, (e) gap mode generated in the nanogap between a metal particle and a metal film, and (f) Fano resonance induced by the interaction between a narrow discrete state and broad continuum.

2. Resonance modes in plasmonic nanostructure arrays

SPR is the resonant oscillation of the conduction electrons in metallic nanostructures.[55–58] This

oscillation can be activated through external electromagnetic (EM) radiation, whose frequency matches the natural resonant frequency of the conduction electrons residing on the metal surface. SPR can be categorized into two fundamental and distinct forms: LSPR and SPPs. LSPR is the non-propagating collective oscillation of surface electrons in metallic nanostructures with dimensions smaller than the wavelength of the incident light. In contrast, SPPs represent propagating charge oscillations along the interfaces between metals and dielectrics. SPPs cannot be excited solely through free-space radiation—prism couplers or grating couplers are required to impart additional momentum, thereby satisfying the momentum-matching condition.[38,52,59] By controlling the morphology and structural parameters of the nanoarchitecture, the coupling and interaction of LSPR and SPPs modes can result in other plasmon modes, such as the F–P cavity mode, SLR mode, gap plasmon mode, and Fano resonance mode.

2.1 Localized surface plasmon resonance (LSPR)

LSPR is a surface phenomenon generated through metal nanoparticles, in which electrons oscillate collectively in resonance with the incident light (Figure 1a). The electric field surrounding the localized plasmons is amplified by several orders of magnitude, and the intensity decays exponentially with distance. These resonances generate sharp optical absorption or scattering as well as strong EM fields. The corresponding scattering cross section (C_{sca}) and absorption cross section (C_{abs}) are expressed as[57,60]

$$C_{sca} = \frac{8}{3}\pi k^4 r^6 \left| \frac{\varepsilon_{\mathrm{m}} - \varepsilon_d}{\varepsilon_m + 2\varepsilon_d} \right|^2, \tag{1}$$

$$C_{abs} = 4\pi k r^3 \,\mathrm{Im}\left[\frac{\varepsilon_{\mathrm{m}} - \varepsilon_d}{\varepsilon_m + 2\varepsilon_d} \right], \tag{2}$$

where k (= $2\pi/\lambda$) represents the wave vector of the incident light, r and ε_m denote the radius and dielectric function of the nanoparticle, respectively, and ε_d symbolizes the dielectric constant of the surrounding environment. At the minimum $|\varepsilon_m + 2\varepsilon_d|$, C_{sca} and C_{abs} attain their maximum values, thereby causing sharp absorption and scattering peaks in the LSPR spectrum of the nanoparticle.

Equations (1) and (2) clearly suggest that the absorption is proportional to r^3 and that the scattering is proportional to r^6. As the sum of absorption and scattering, the extinction is dominated by the scattering effect for large nanoparticles and by the absorption effect for small nanoparticles.[39] In addition, LSPR is greatly influenced by the size and composition of the nanoparticles as well as the dielectric constant of the surrounding environment.

2.2 Propagating surface plasmon polaritons (SPPs)

SPPs are evanescent electromagnetic (EM) surface waves that propagate at an extended continuous metal-dielectric interface (Figure 1b). In accordance with Maxwell's equations, the SPPs dispersion relation (K_{spp}) can be expressed as[57,61]

$$K_{\mathrm{spp}} = \frac{\omega}{c}\sqrt{\frac{\varepsilon_m \varepsilon_d}{\varepsilon_m + \varepsilon_d}}, \tag{3}$$

where ε_m denotes the dielectric function of the metal and ε_d indicates the dielectric constant of the surrounding environment. The nonlinear nature of SPPs results in a momentum mismatch between the incident light and SPPs, which can be overcome if[38]

$$\varepsilon_m + \varepsilon_d = 0 \tag{4}$$

Generally, momentum mismatch is compensated through adopting prism coupling, grating coupling, and near-field coupling, which grant additional momentum to the light.[62–64] In particular, the penetration depth of an EM field in a dielectric is usually greater than that in a metal, which is more prominent at longer wavelengths.[65]

2.3 Fabry–Pérot (F–P) cavity mode

Generally, F–P cavity modes occur in thin films comprising two metallic mirrors separated by an optically transparent dielectric medium (refer to Figure 1c), in which constructive interference of EM waves may occur in the dielectric cavity.[40,66] When the propagation direction of the incident light is perpendicular to the resonator planes, the wavelength of the N^{th} mode (λ_N) can be calculated as [67]

$$\lambda_N = \frac{2n_d(d+\delta)}{N}, \tag{5}$$

where n_d indicates the real part of the refractive index of the dielectric coating, d denotes the thickness of the dielectric between the two gold mirrors, and δ represents the increased cavity length owing to the reflection phase. Notably, the resonance wavelength of the F–P cavity is highly dependent on the cavity thickness.

Furthermore, the effective cavity mode volume (V_{mode}) is another critical parameter of optical resonators, representing the EM field trapped in the F–P cavity. This parameter is defined as the ratio of the total stored EM energy to the maximum EM energy density, as follows[68,69]:

$$V_{\text{mode}} = \frac{\iiint \varepsilon(\vec{r})\left|\vec{E}(\vec{r})\right|^2 d^3\vec{r}}{\max\left\{\varepsilon(\vec{r})\left|\vec{E}(\vec{r})\right|^2\right\}}, \tag{6}$$

where $\varepsilon(\vec{r})$ indicates the dielectric constant and $E(\vec{r})$ symbolizes the electric field strength. The F–P resonance can manipulate the electric field distribution and may generate a strong electric field inside the cavity. Therefore, when photoactive materials are placed inside the F–P cavity, their absorption is modulated via the F–P resonance effect.[70]

2.4 Surface lattice resonance (SLR) mode

SLR is the enhanced interaction in periodic nanoparticle arrays through near-field coupling and far-field coupling (refer to Figure 1d), which originates from LSPR coupling with diffractive waves of the array.[71,72] SLR, alternatively named the collective resonance, suppresses the radiative damping of plasmonic resonance. The quality and linewidth of the SLR can be tuned over the UV-vis-NIR spectrum by varying the array period, arrangement, particle size, material, position, size disorder, and the surrounding refractive environment.

The method of coupled-dipole approximation effectively illustrates the properties of SLR. Each metal nanoparticle is considered a dipole with $\vec{P}_i = \alpha_i \vec{E}_i$, where α_i denotes the

polarizability of the i^{th} particle and $\vec{E}_i$ indicates the corresponding local field. Notably, the α of each metal particle can be considered identical for infinite plasmonic arrays. The effective polarizability (α_{eff}) and extinction cross-section (C_{ext}) of each particle in the arrays are expressed as[72,73]

$$\alpha_{\text{eff}} = \frac{1}{\left(\frac{1}{\alpha_s} - S\right)}, \tag{7}$$

$$C_{ext} = 4\pi k N \,\text{Im}(\alpha_{\text{eff}}), \tag{8}$$

where α_s indicates the polarizability of an isolated metal particle, S represents the sum of the dipoles retarded from other particles, N denotes the number of particles, and k symbolizes the wavenumber of the incident light. The intriguing phenomenon of redistribution of the EM field is associated with an incident wave through diffractive coupling from ordered plasmonic arrays, causing the field to concentrate near the plane of the array. Compared to the optical absorption attributed to the LSPR effect of a single nanoparticle, the SLR from nanoparticle arrays exhibits a narrower optical spectrum and a stronger local field. Considering SLR's advantageousness, this mode is favorable for ultrasensitive sensing applications, new metamaterials, improved photovoltaic cells, and highly efficient photocatalysis.

2.5 Gap plasmon mode

Surface plasmons that confine a high EM energy within a nanogap between neighboring metallic nanostructures are defined as gap plasmons (refer to Figure 1e). In this structure, near-field coupling is dominant, confining the EM field through the high localization of light energy into a compact space.[74–76] Compared with a single nanoparticle, the resonance wavelength of the nanoparticle in the gap mode exhibits a redshift in the presence of an adjacent metal nanostructure, thereby weakening the restoring force acting on the electrons of the structure.[74,77] If the space layer is extremely thin (typically < 8 nm), then the gap plasmon is considerably intense owing to strong light confinement.[38] Because the EM field strength of the gap plasmon decreases with an increase in the thickness of the spacer layer, fine control of the distance is crucial for manipulating the gap mode. Additionally, unlike the LSPR mode, in which the EM field decays exponentially with distance, the gap mode causes the EM energy to oscillate between the magnetic and electric counterparts inside the gap, rendering an approximately uniform EM field intensity over the entire gap.[38] Therefore, the high enhancement of the plasmon intensity in the gap mode is beneficial for energy transfer, sensing, and solar energy harvesting.

2.6 Fano resonance mode

The Fano resonance originates from quantum interference phenomena, which exhibit a narrow asymmetric spectral shape with resonant suppression and enhancement induced by the interaction between a narrow discrete state and a broad continuum (refer to Figure 1f). This phenomenon was observed in plasmonic nanostructures with symmetry breaking or clusters of plasmonic nanoparticles.[40,78–81] In this process, the suppression and enhancement of resonance are induced by the destructive or constructive interference of the two modes, respectively. The

absorption spectrum shape of the Fano resonance is given by[82]

$$\sigma(E) = D^2 \frac{(q+\Omega)^2}{1+\Omega^2}, \quad (9)$$

where E denotes the energy, D represents the non-resonant transfer amplitude ($D^2 = 4\sin^2\delta$), $q = \cot\delta$ indicates the shape parameter determining the asymmetry of the profile, δ symbolizes the phase shift of the continuum, and $\Omega = \frac{2(E-E_0)}{\Gamma}$ (Γ denotes the resonance width, and E_0 indicates the resonance energy). Hence, the resulting shape of the absorption spectrum of the Fano resonance describes the superposition of the two modes. Owing to the narrow bandwidth and enhanced near-field of Fano resonance, light is efficiently confined at the desired frequency. In particular, this mode has been applied to plasmonic sensors, lasing, medicine, metamaterials, and optoelectronic devices.[82–85]

3. Nanostructure designs and fabrication methods

Generally, nanostructures are categorized into four groups: zero-dimensional (0D; such as nanodots, nanoparticles, and nanocubes), one-dimensional (1D; such as nanowires, nanorods, and nanoneedles), two-dimensional (2D; such as nanosheets and patterned surfaces), and three-dimensional (3D; such as nanocones and nanopillars) nanostructures.[86,87] Accordingly, ordered nanostructure arrays are classified into four types (0D, 1D, 2D, and 3D nanostructure arrays) based on the morphology of the individual nanostructure, as illustrated in Figure 1. Herein, we present the design and fabrication method of each group separately, and subsequently, explore their applications in solar-to-chemical energy conversion.

Photolithography, implemented with photomasks, is the most widely used technique in the nanoscale fabrication industry to form exposure patterns. However, this technology is limited in terms of its low resolution resulting from its diffraction-limited resolution (approximately $\lambda/2$, where λ indicates the wavelength). Consequently, the fabrication of metallic plasmonic arrays with high-quality nanoscale features is a difficult task.[38] New nanofabrication techniques have been developed to overcome these challenges, including self-assembly colloidal lithography, nanoimprint lithography, and anodic aluminum oxide (AAO) template-based lithography. Essentially, an ideal nanofabrication technique should grant adequate flexibility for tailoring the nanostructure size and shape at a low cost, high throughput, and high resolution.

3.1 Nanosphere lithography

The nanosphere lithographic method, based on self-assembled colloidal spheres, is an alternative strategy for generating periodic nanostructures without complex equipment. As presented in Figure 2 (a–c), spherical colloids are transferred to close-packed structure patterns through capillary forces during the process. By using etched self-assembled colloidal spheres as templates or masks, a wide range of 2D arrays of nano-objects (e.g., triangular particles, nanodots, nanoholes, nanodisks, nano bowls, hollow spheres/shells, nanorings) and 3D nanostructures (e.g., cones, pyramids, and pillars) can be fabricated onto substrates[44] via reactive ion etching (RIE), electron beam irradiation, thermal/e-beam deposition, sputtering

deposition, atomic layer deposition (ALD), and pulsed laser deposition (PLD). The morphology and arrangement of the nanostructure can be easily regulated by altering the bead size and etching process. However, this method generally produces nanostructures in hexagonal arrangements, which are inherited from hexagonal colloidal sphere arrays in accordance with the principle of minimum energy in the self-assembly process.

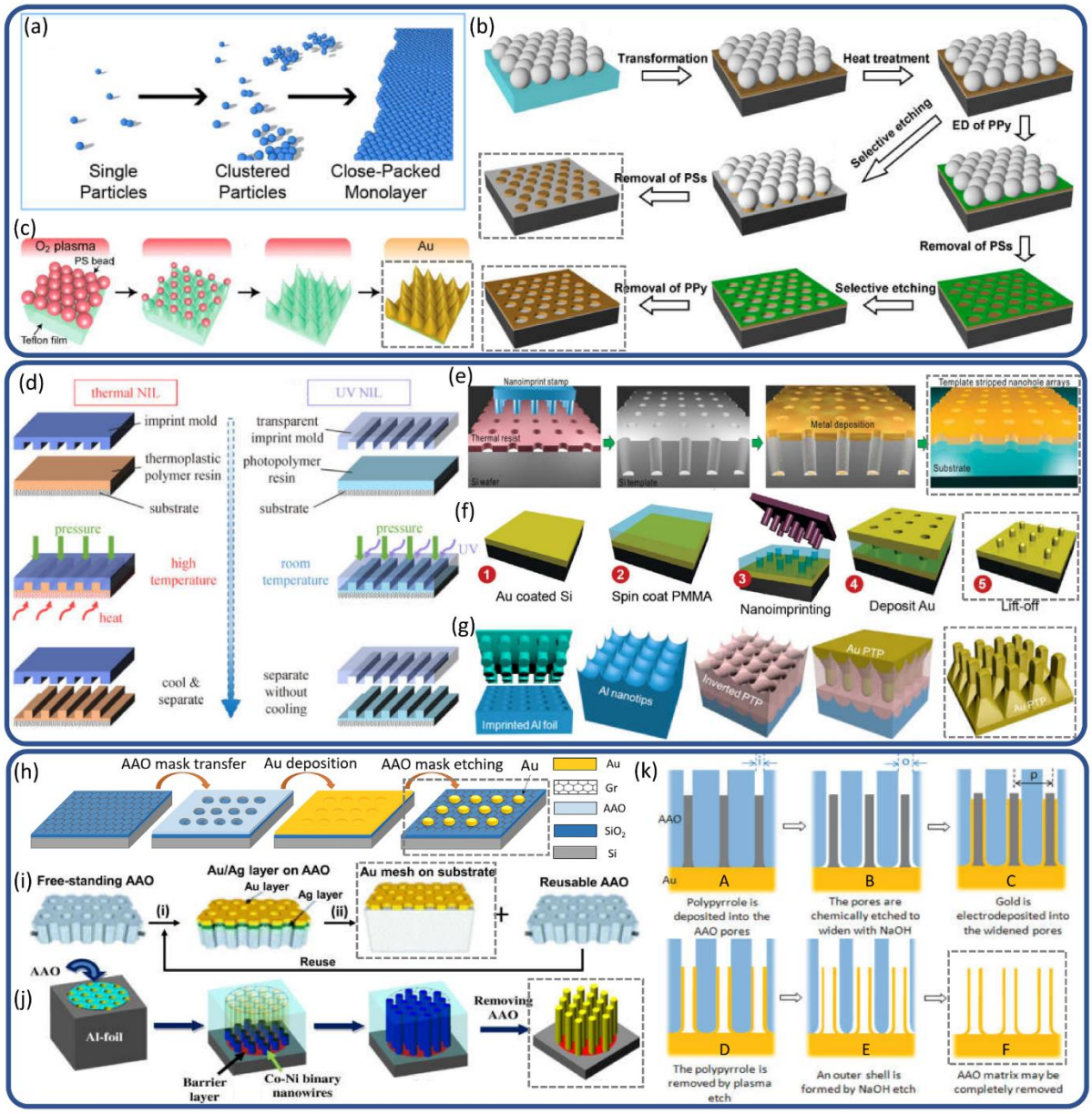

Figure 2. Schemes of lithography techniques for the fabrication of metallic plasmonic arrays. (a) Self-assembly of colloidal particle structures to form a hexagonal close-packed array.[88] Fabrication of (b) Au nanodisk, nanohole, Reproduced with permission.[89] Copyright 2014, American Chemical Society. and (c) nanocone arrays. Reproduced with permission.[90] Copyright 2013, American Chemical Society. (d) Conventional nanoimprint lithography (NIL): thermal NIL, ultraviolet NIL, and replication performance. Reproduced with permission.[91] Copyright 2021, Springer Nature. Fabrication procedures for large-area (e) nanohole arrays, Reproduced with permission.[92] Copyright 2011, American Chemical Society. (f) nanopillar arrays, Reproduced with permission.[93] Copyright 2012, American Chemical Society. and (g) Au pillar/truncated pyramid arrays. Reproduced with permission.[94] Copyright 2017, American Chemical Society.AAO template is used to fabricate (h) nanodot arrays, Reproduced with permission.[95] Copyright 2019, Springer Nature. (i) nanohole arrays, Reproduced with permission.[96] Copyright 2013, Royal Society of Chemistry. (j) nanowire arrays,[97] and (k) nanotube arrays.

Reproduced with permission.[98] Copyright 2010, American Chemical Society.

3.2 Nanoimprint lithography

Nanoimprint lithography (NIL) is a promising approach for mechanically pressing a prefabricated stamp with a designed pattern onto various substrates, owing to its ease-of-use and accessible resolutions below 10 nm.[99,100] This technique, first proposed by Chou's *group*[101,102], is considered the most promising fabrication technology for high-throughput patterning of nanostructures owing to its merits in terms of low cost, large-area fabrication, and high fidelity. As presented in Figure 2 (d), two subsequent nanoimprint processes are commonly employed: thermal NIL and UV NIL.[91,103] In this process, a stamp (or mold) with a specific pattern is mechanically pressed into the coated imprint fluid on a substrate, and the pattern is transferred into the imprint fluid. After thermal curing or UV light exposure hardening, the stamp is removed, rendering a nanostructure pattern on the substrate. As molds are utilized in NIL to form nanostructures, the minimum feature size of the nanostructure pattern primarily depends on the feature size of the mold pattern. As depicted in Figure 2 (e-g), arrays of nanoholes, nanopillars, and pillars/truncated pyramids can be fabricated using this method.

3.3 Template-directed techniques

AAO templates and ultrathin alumina membranes (UTAM) were fabricated by metal anodization in acidic solutions to form periodic metal oxide nanopores.[104,105] They are widely used as templates to assist in nanopatterning. Template-directed techniques are advantageous in terms of low cost, high resolution, a high aspect ratio, and optimal repeatability. However, the geometry and layout of the nanostructures are limited by the structural parameters of the AAO template and brittleness of the operating process.[38,106] Reportedly, the AAO template allows for easy manipulation of the pore diameter (D_p = 20 – 400 nm), interpore distance (D_{int} = 60 – 500 nm), pore density (ρ = 108–1010 cm^{-2}), and pore shape by simply controlling the electrochemical conditions, such as electrolytes and voltages, or by adopting a prepatterned aluminum substrate.[96,107,108] The detailed procedure is illustrated in Figure 2 (h). This technique has been applied to fabricate a wide range of nanostructure arrays, ranging from 0D to 3D configurations, such as nanodot arrays, nanohole arrays, nanopillar arrays, and nanotube arrays.[41,49,109,110]

Table 1 summarizes and compares the different fabrication techniques presented in this section. Each technique has its advantages and challenges. As plasmon modes are highly dependent on the nanoarchitecture, selecting the proper fabrication technique is essential for generating and modulating the geometry and optical properties.

Table 1. Summary and comparison of different fabrication techniques in terms of feature sizes, advantages, challenges, and nanostructure arrays.

Fabrication method	Minimum feature size	Advantages	Challenges	Nanostructure arrays	Dimension
Nanosphere lithography	Sub-100 nm [111]	Flexible, low cost, and extremely high throughput	Inevitable defects	Nanoparticle,[112] triangular particle,[113] nanohole,[114–116] nanodisk,[89] nanobowl,[117,118] nanoring,[119] half-shell,[120]	0D 2D 3D

				nanocone,[35,90] and nanopyramids[121,122]	
Nanoimprint lithography	Sub-10 nm [123–125]	High throughput	Morphology limited by stamp	Nanodot,[126] nanosphere,[127] nanohole,[92,128] nanoring,[129] and nanopillar[93]	0D 2D 3D
Template-directed techniques	5 nm [130,131]	High throughput	Difficult to generate long-range–ordered periodic nano-array patterns	Nanodot,[95,132,133] nanoparticle,[134,135] nanowire,[97,136–138] nanomesh,[96,139] nanohole,[140] nanotube, [98] and 3D nanostructure[94,141]	0D 1D 2D 3D

4. Applications of solar-to-chemical energy conversion

4.1 Mechanisms of SPR-enhanced photocatalysis

The plasmonic metal nanostructures feature resonant excitation of plasmons and an intensive local EM field near the surface, which are attributed to the SPR effect. By cooperating with semiconductor photocatalysts, plasmonic metal nanostructures exhibit enhanced light trapping and an EM field at the metal–semiconductor interface. Figure 3 plots the time evolution of the plasmon decay process and different mechanisms of plasmonic nanostructures coupled with semiconductors. During the plasmon decay process, intense local EM fields near the surface of metal nanostructures interact with semiconductors through either (a) local electromagnetic field enhancement (LEMF) or (b) plasmon-induced resonant energy transfer (PIRET).[26,52] Moreover, the excited surface plasmons decay either radiatively through the re-emission of photons or non-radiatively by transferring energy to hot electrons and holes. In the radiative process, the incident light can be partially scattered into the semiconductor via (c) the light-scattering mechanism, thereby increasing the optical path length. In the non-radiative process, the hot carriers redistribute their energy through electron–electron scattering (100 fs–1 ps), electron–phonon scattering (1 ps–10 ps), and phonon–phonon scattering (100 ps–10 ns) processes.[23,142,143] During the aforementioned decay processes, the hot carriers are transferred to semiconductors via (d) HEI, competing with electron relaxation on time scales of hundreds of femtoseconds. Alternatively, the hot carriers may relax by locally heating the nanostructure via (e) the plasmonic heating effect. Table 2 summarizes the features of the five different mechanisms for plasmonic nanostructures coupled with semiconductors.

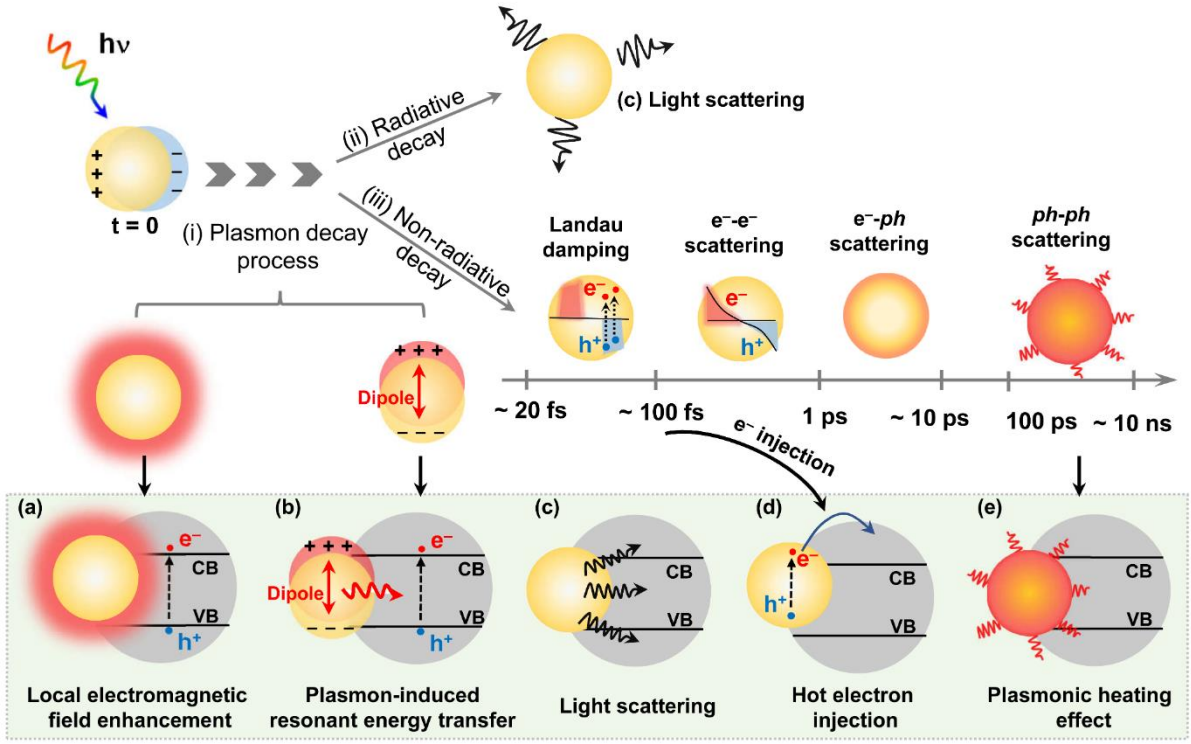

Figure 3. Plasmon decay process and the different mechanisms for plasmonic nanostructure coupled with semiconductors comprising (a) local electromagnetic field enhancement (LEMF), (b) plasmon-induced resonant energy transfer (PIRET), (c) light scattering, (d) hot-electron injection (HEI), and (e) photothermal heating effect.

Table 2. Summary of plasmonic nanostructure coupled with semiconductors.

Mechanisms	Feature	Role
LEMF	Near-field effect; larger SPR energy than the band gap or intraband gap of semiconductors.	Enhances the charge-carrier formation rate of semiconductors.
PIRET	Non-radiative energy-transfer mechanism; absorption spectral overlap of SPR and semiconductor.	Realizes the upward energy transfer.[26]
Scattering	Far-field effect; larger SPR energy than the band gap or intraband gap of semiconductor.	Lengthens the light pathway within the semiconductor; enhances the charge-carrier formation rate of semiconductors.
HEI	Short lifetime of excited carriers, intimate contact between metal and semiconductor; higher hot-electron energy than the Schottky barrier.	Extends the absorption range of semiconductors.
Photothermal heating effects	Increased temperature of the surrounding medium owing to the thermal equilibrium of lattice phonons; more efficient in small nanostructures.	Utilized for thermal activation of chemical reactions.

Owing to the strong correlation between the EM field and hot electron-based plasmonic enhancement, the localized EM field can be amplified to boost the hot electron-mediated catalytic efficiency. Plasmonic “hot spots” are areas with highly inhomogeneous and

significantly enhanced EM fields in sharp corners, tips, or gaps between nanostructures separated by a few nanometers.[144][145] Research has revealed that the local EM field near the hot-spot region can yield multiplied or exponential enhancement, which can drastically increase the probability of generation and collection of hot electrons.[146] Additionally, Govorov *et al.* modeled the generation of plasmonic hot carriers based on quantum theory; they concluded that the scattering of electrons through nanocrystal surfaces and hot spots can impart more high-energy hot electrons.[145,147–151] In particular, the generation rate of high-energy hot electrons capable of crossing the Schottky barrier was theoretically formulated using different degrees of approximation. This rate is formulated as the following integral:[148]

$$\text{Rate}_{\text{HE,over-barrier}} = \frac{2}{\pi^2} \times \frac{e^2 {E_F}^2 \left(\hbar\omega - \Delta E_b\right)}{\hbar(\hbar\omega)^4} \times \int_S \left| E_{normal}(\theta \cdot \varphi) \right|^2 dS \,, \tag{10}$$

where ω denotes the photon frequency, ΔE_b indicates the barrier height, E_F represents the Fermi level of the metal, $E_{normal}(\theta \cdot \varphi)$ symbolizes the normal component of the internal electric field near the metal nanocrystal surface, and the integral is calculated over the entire surface S. The increased generation rates of energetic electrons are attributed to the classical plasmon enhancement effect and quantum phenomenon corresponding to the non-conservative linear momentum of electrons in the confined system[152], which is favorable for photocatalytic applications.

4.2 Applications of plasmonic nanostructure arrays in photocatalysis

4.2.1 0D nanostructure arrays

Metal nanoparticles facilitate LSPR excitation via coherent oscillations of free electrons. The tunable optical response can be tailored by changing the size, shape, and material of nanostructures.[153,154] LSPR can lead to large local EM-field enhancements in deep sub-wavelength volumes, and their near fields can couple and further confine the field when the nanoparticles are in close proximity.[155–157] Compared to individual or disordered nanoparticles, metal nanoparticle arrays with spacings comparable to the wavelength of light can generate large field enhancements and high-quality resonances by leveraging short- and long-range interactions.[46,158]

Kim *et al.* prepared size-controllable Au nanodot arrays using a direct contact printing method to investigate the size effect of Au nanodots on water photoelectrolysis.[126] The schematic illustrations in Figure 4 (a–d) depict the entire fabrication process of the TiO_2-coated Au nanodot arrays. As illustrated in Figure 4 (e), with a decrease in the size of the Au nanodot, the LSPR peak energy (E_{LSPR}) increases, whereas the LSPR linewidth (Γ) decreases, leading to a larger local field enhancement and a higher quality factor Q (= E_{LSPR}/Γ). Consequently, the photoelectrocatalytic (PEC) water-splitting reaction is more efficient because of the generation of a greater number of charge carriers. The Faradaic efficiencies of the TiO_2-coated 50-nm Au nanodot and 50-nm Au nanodot arrays are 94.9% and 92.8%, respectively, indicating that most of the photo-induced charge carriers on the Au nanodots participated in the water splitting reaction. The hydrogen production rate of the TiO_2-coated 50-nm Au nanodot array is

approximately five times higher than that of the uncoated ones, as demonstrated in Figure 4 (f).

With regard to the core/shell structure of metal/semiconductor contacts, metallic nanostructured cores or shells can introduce SPR effects into the relevant devices; thus, the collection of generated charge carriers can be enhanced based on this introduction.[109] Zhan *et al.* established an ideal model system to exclusively study the effect of nanoparticle height on the SPR property in ordered plasmonic metallic nanoparticle arrays (Ag and Au).[134] Scanning electron microscopic (SEM) images of uniform Au nanoparticle arrays coated with a TiO_2 shell (thickness of ~ 22 nm) are shown in Figure 4 (g). As observed in the UV-vis-NIR extinction spectra in Figure 4 (h), the major SPR peaks (dipole mode) of the Ag nanoparticle arrays exhibit an obvious peak-narrowing effect and a continuous blue shift with increasing height. In comparison, three types of higher-order multipole SPR modes (quadrupole at ~510 nm, octupole at ~460 nm, and hexadecapole mode at ~350 nm) exhibit a gradual increase from zero to strengthening. With a further increase in the height from 75 to 155 nm, the peak intensity of the multipole modes increases considerably, whereas the peak of the dipole SPR mode exhibits minor changes in its position, intensity, and width. As demonstrated by the photocurrent responses of Ag@TiO_2 in Figure 4 (i), the photocurrents rise with the height of Ag nanoparticles, and the photoocurrent of Ag (155 nm) @TiO_2 approaches approximately 90 $\mu A\ cm^{-2}$, which is approximately 40 times higher than that of pure TiO_2 samples. Furthermore, systematic research revealed that multipole SPR modes significantly contribute to photocarriers, and in particular, the SPR parameters (position, intensity, mode, etc.) of metallic nanoparticle arrays can be tuned in broad UV-vis-NIR regions by changing the heights.

Moreover, Zhan *et al.* reported an approach to enhance the SPR performance of ordered plasmonic Ag nanoparticle arrays by accurately controlling the thickness of the coated TiO_2 shells, in which dipole and quadrupole SPR modes were manipulated to coincide with each other.[159] The fabricated highly ordered Ag nanoparticle arrays are illustrated in Figures 4 (j) and (k). Additionally, the variations in the dipole and quadrupole SPR modes of the Ag@TiO_2 nanocapsule structures are displayed in Figure 4 (l): the quadrupole SPR mode overlaps with the dipole mode. As presented in Figure 4 (m), the Ag@TiO_2 nanocapsule structures exhibit a significantly higher photocurrent response than the bare TiO_2 layers. Observably, the Ag@TiO_2 nanostructure with a shell thickness of 25 nm exhibits the best performance, and its photocurrent can reach 83 $\mu A\ cm^{-2}$, which is ~38 times higher than that of the same TiO_2 layer. This indicates that the degeneracy of the dipole and quadrupole SPR modes of ordered Ag nanoparticle arrays can be controlled by adjusting the thickness of TiO_2, which induces enhanced plasmon-mediated LEMF and HEI effects and enhances the generation of photo-induced charge carriers for solar energy conversion. Similarly, a self-assembled bilayer film fabricated by Sun *et al.* yielded optimal behavior using an Au@ZnO core–shell nanoparticle (NP) array with a 25-nm shell thickness. This fabrication demonstrated a synergistic effect when the plasmatic NPs core acted as the visible light absorber and the semiconductor shell as the photocatalyst.[160]

To characterize the lateral coupling effect between neighboring nanoparticles, Wu *et al.* fabricated hexagonal close-packed Au/TiO_2 nanocrystal arrays (NCAs) with highly ordered periodicity and uniformity.[112] Figure 4 (n) depicts an SEM image of the ordered periodicity of the Au NCAs, with the Au particles located in the middle of the honeycomb SiO_2 walls. The normalized measured scattering spectra of the NCAs obtained via far-field optical spectroscopy

are displayed in Figure 4 (o). The λ_{LSPR} of bare Au NCAs is approximately 575 nm, whereas the Au/TiO_2 NCAs exhibit two λ_{LSPR} peaks because they are encircled partly by TiO_2 and SiO_2. As shown in Figure 4 (p), the hydrogen production of the Au/TiO_2 NCAs is significantly higher than that of the randomly distributed Au/TiO_2 nanocomposites. By increasing the Au core, as presented in Figure 4 (q), the H_2 production efficiency of the Au core (110 nm)/TiO_2 NCAs is higher than that of the Au core(100 nm)/TiO_2 NCAs. Moreover, the corresponding mapping of the cross-section near-fields in Figures 3 (r) and (s) reveals that the electric field of the Au core/TiO_2 NCAs is enhanced at interfaces along all directions, and the lateral coupling increases in strength when the Au core is enlarged with the spacing remains unchanged. Owing to the highly ordered periodicity, both the enhanced electric field and lateral coupling in Au/TiO_2 NCAs contributed to the higher photocatalytic activity in this work. Furthermore, Lei's group fabricated a library of Au NP superlattices comprising two or three subsets of NPs that exhibited multiple plasmonic resonances by systematically tuning the size and height of each subset of NPs. By embedding the Au NP superlattice in the photoanodes, a large improvement of approximately 260% was achieved compared to that of the bare film reference.[161]

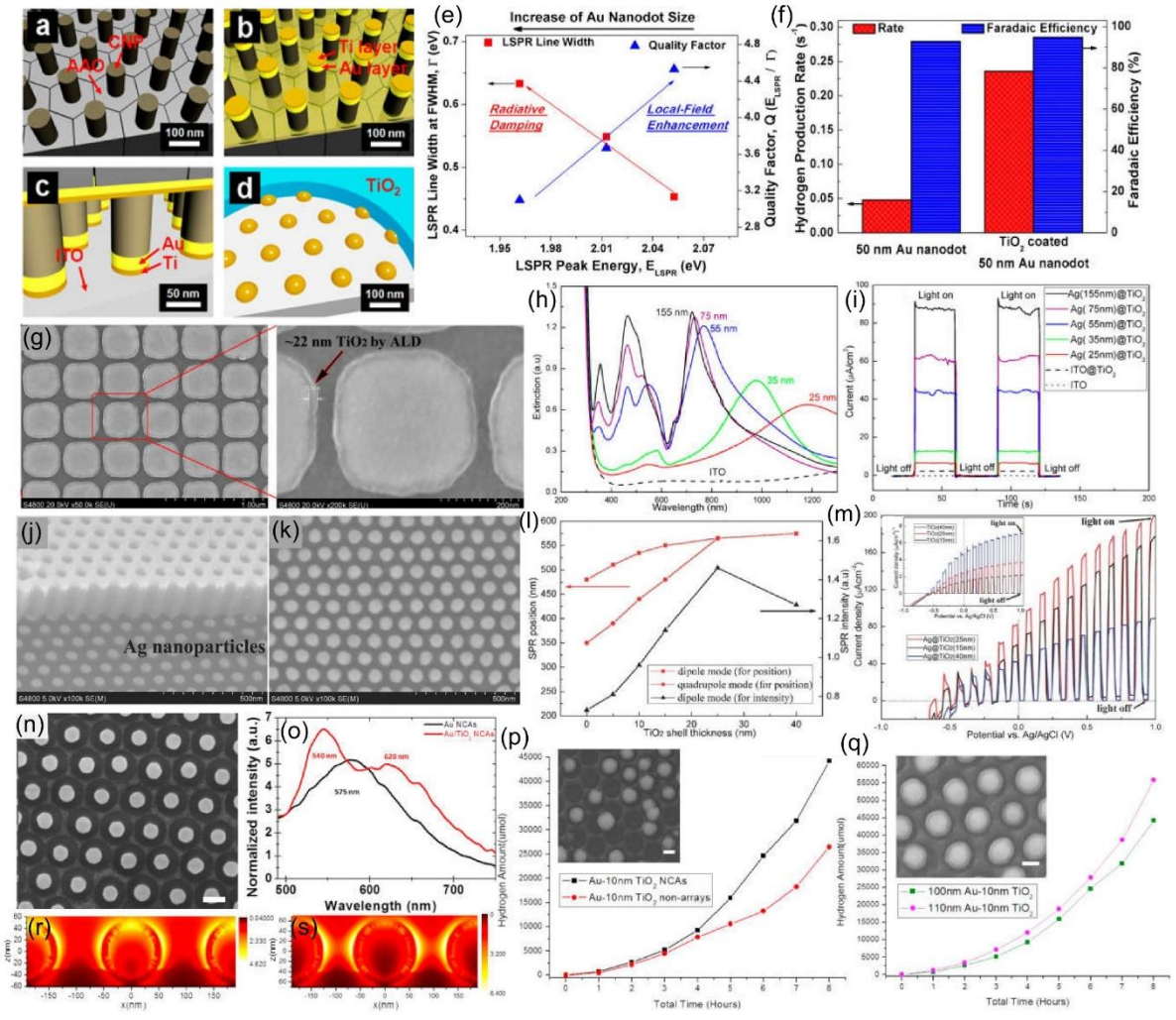

Figure 4 (a-d) Fabrication process of TiO_2-coated Au nanodot arrays. (e) Dependences of the LSPR linewidth and quality factor ($Q = E_{LSPR}/\Gamma$) on the LSPR peak energy as obtained from the UV-vis measurements. (f) Hydrogen

production rate and Faradaic efficiency after light irradiation for 1 h. Reproduced with permission.[126] Copyright 2014, American Chemical Society. (g) Top-view SEM images of Au nanoparticle arrays after the coating of a thin shell of TiO_2 with a thickness of ~22 nm via ALD. (h) Experimental UV-vis-NIR extinction spectra of Ag nanoparticle arrays deposited onto ITO-coated glasses with heights of about 25, 35, 55, 75, and 155 nm. (i) Photocurrent responses of Ag samples to the repeated on/off cycles of AM 1.5 light illumination. Reproduced with permission.[134] Copyright 2015, American Chemical Society. (j) Perspective and (k) top-view SEM images of ordered and uniform Ag nanoparticle arrays fabricated using the ultrathin alumina membrane (UTAM) technique. (l) Variation of dipole and quadrupole SPR modes of Ag@TiO_2 nanocapsule structures with different TiO_2 shell thicknesses. (m) Photocurrent responses of Ag@TiO_2 nanocapsule structures and the same TiO_2 layers on ITO substrates under the illumination of a chopped AM 1.5 light. Reproduced with permission.[159] Copyright 2015, John Wiley & Sons, Inc. (n) Top-view SEM images of the hexagonal close-packed nanocrystal arrays (NCAs). (o) Measured scattering spectra of the Au NCSs with 100-nm Au and the Au/TiO_2 NCAs with 10-nm TiO_2. (p) Amounts of hydrogen produced by the Au/TiO_2 NCAs and randomly distributed Au/TiO_2 nanoparticles under visible light irradiation. Inset is the SEM image of randomly distributed Au/TiO_2 nanoparticles. (q) Amounts of hydrogen produced by the Au/TiO_2 NCAs with the same thickness (10 nm) of TiO_2 but larger Au core (110 nm) under visible light irradiation. Inset is the SEM image of 110-nm Au core /TiO_2 NCAs. The mapping of cross-section near-fields for NCAs of (r) Au core (100 nm)/TiO_2 and (s) Au core (110 nm)/TiO_2 partially immersed in SiO_2 simulated through finite-difference time-domain (FDTD). Reproduced with permission.[112] Copyright 2016, Elsevier.

In addition to the direct interaction with semiconductors, nanoparticle arrays have a diffraction mode that couples with the LSPR of individual nanoparticles to support SLRs. Deng *et al.* reported strongly coupled bimetallic core–shell nanoparticle arrays that showed excellent PEC activity for hydrogen evolution reactions (HER).[162] Cu−Pt nanoparticle lattices were fabricated by combining top-down lithography and solution-based chemistry, as shown in Figure 5 (a). The experimental transmission spectra of the Cu@Pt nanoparticle lattices and the spectral ranges of the different wavelengths are illustrated in Figure 5 (b). Blue, orange, and IR illumination lights were utilized to probe the contributions of Cu interband transition, localized surface plasmons (LSPs), and SLRs, respectively. As presented in Figure 5 (c), the Cu nanoparticle lattices under IR wavelengths exhibit a reaction rate higher than that under blue or orange light, and the corresponding slope of the catalytic activity is approximately twice that under orange light, indicating a stronger enhancement of activity from the SLRs. In comparison, the Cu@Pt nanoparticle lattices depicted in Figure 5 (e) exhibit an even higher catalytic activity enhancement, which is attributed to stronger light absorption and more intense EM fields, considering that the Pt nanoparticle lattices exhibit a weak dependence on light wavelengths, as presented in Figure 5 (d). In particular, the SLRs from the bimetallic core–shell nanoparticle lattices generated higher near-field intensities and stronger light absorption than the LSPs, which further enhanced the plasmonic PEC activity. Notably, the scalable and tunable core–shell nanoparticle lattices would provide a promising platform for boosting PEC processes in cavities by controlling both resonant energy and chemical reactivity, thereby enabling exquisite manipulation of the coupling strength of light–matter interactions at the nanoscale.

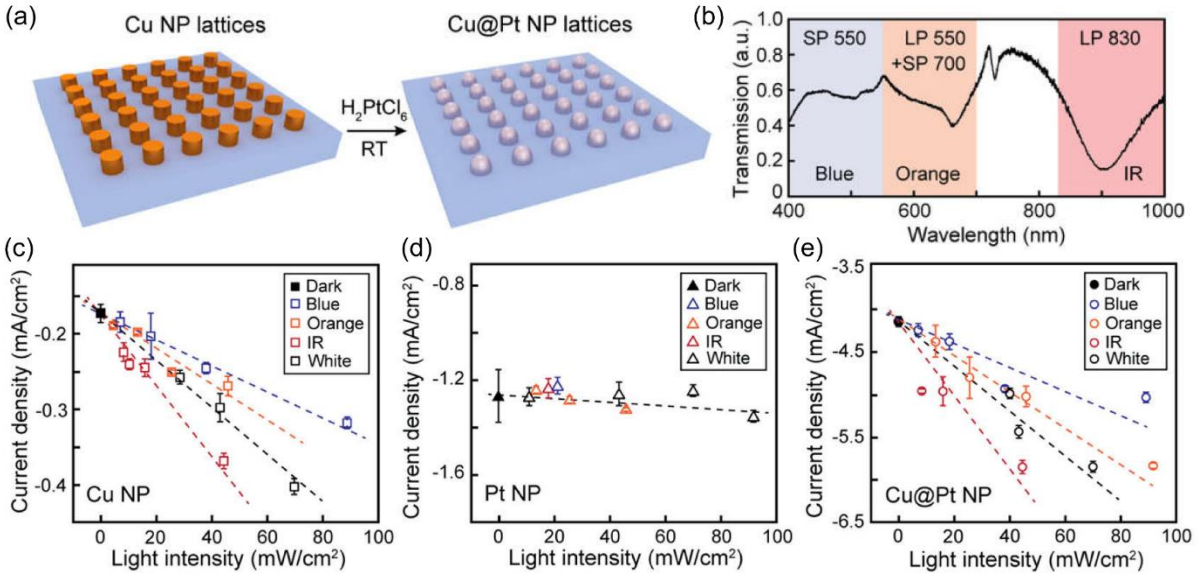

Figure 5 (a) Fabrication scheme of Cu@Pt nanoparticle lattices based on Cu nanoparticle lattices. RT = room temperature. (b) Experimental transmission spectra of Cu@Pt nanoparticle lattices and spectral ranges of different illumination lights. Current density vs. light intensity of (c) Cu nanoparticles, (d) Pt nanoparticles, and (e) Cu@Pt nanoparticle lattices with a bias potential of −0.2 V vs. RHE. Reproduced with permission.[162] Copyright 2021, American Chemical Society.

4.2.2 1D nanostructure arrays

The large surface area and efficient charge conduction in 1D metallic nanostructure arrays greatly facilitate PEC reactions. In this regard, Lee *et al.* designed a plasmonic water-splitting cell in which the aligned gold nanorods were capped with TiO_2 to form a Schottky metal–semiconductor interface.[163] A schematic of the fabrication of the Au/TiO_2 nanostructures and working cell is shown in Figures 6 (a) and (b). High-resolution transmission electron micrographs (TEM) of a typical Au nanorod after TiO_2 deposition and Co-OEC electrodeposition are illustrated in Figure 6 (c). The photocurrent versus time plot in Figure 6 (d) demonstrates that the photocurrents are significantly enhanced under visible light illumination compared to those under UV illumination. As depicted in Figure 6 (e), two pronounced LSPR peaks are observed at 508 and 610 nm under visible light, corresponding to the transverse and longitudinal modes of plasmonic excitations in the assembly, respectively. Furthermore, the photocurrent action spectra accurately tracked the two surface plasmon extinction bands, indicating that the visible-light response of the device arose from the surface plasmon excitations in the Au nanorods. Reportedly[164–167], the wavelength of the longitudinal mode resonance in the nanorod arrays was strongly dependent on the aspect ratio and interspacing distance of the nanorods. In particular, the interspacing distance in the nanorod arrays was sufficiently short for strong coupling between the nanorods, resulting in a blue shift of the higher-energy absorption peak compared to the isolated longitudinal mode.[168,169] Under illumination, 95% of the effective charge carriers derived from the surface plasmon decayed into hot electrons, and the Faradaic efficiency of the process approached ~80% in ~25 min (refer to Figure 6f).

Considering to the large surface area and attractive surface plasmon decay of Au nanorods, Lee *et al.* designed an autonomous solar water-splitting device, as presented in Figure 6 (g–i).[170] A cobalt-based oxygen evolution catalyst was deposited on the transverse surface of the nanorods, and Pt-decorated TiO_2 was deposited at the end of the nanorods. In their device, TiO_2 acted as an electron filter as well as a support for the Pt nanoparticles, which acted as HER catalysts. The H_2 production rate of the device is plotted in Figure 6 (j). Under UV-dominated illumination ($310 < \lambda < 520$ nm), the H_2 production rate was only 0.2 mmol h^{-1} g^{-1}. By comparison, the H_2 production rate of the device was ~1.14 mmol h^{-1} g^{-1} under the visible light illumination, and this value more than doubled to 2.8 mmol h^{-1} g^{-1} under the full solar spectrum. The efficiency of this autonomous solar water-splitting device, which was based on the Au nanorod array, was attributed to the excited hot electrons from the surface plasmons in the nanostructured Au.

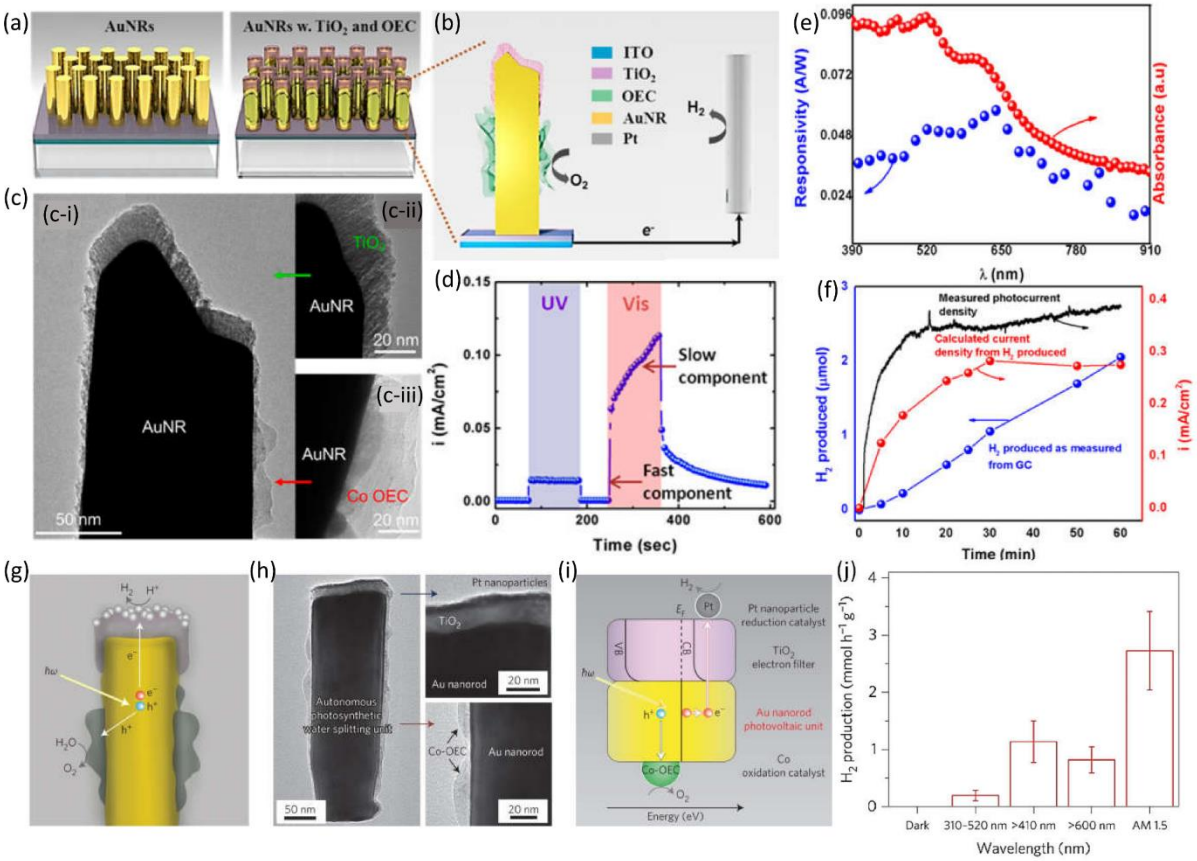

Figure 6. (a) Schematic of the fabrication of Au/TiO_2 nanostructures on an ITO-coated glass. (b) Schematic of the working cell in which only the plasmonic anode is exposed to light. (c) TEM images of a composite plasmonic photoanode (Co–OEC/AuNR/TiO_2) structure (AuNR indicates the Au nanorod). Two distinct areas are observed with the E-beam-deposited TiO_2 on the top of the nanorod (green arrow) and electrochemically deposited Co-OEC layer residing directly on the Au surface (red arrow). Higher magnification images reveal that no Co–OEC was deposited onto the TiO_2, and electrochemical deposition of Co-OEC occurred exclusively on the bare AuNR surfaces. (d) Photocurrent density of the AuNR/TiO_2 with Co-OEC layer. (e) Photocurrent action spectrum (blue) of Co–OEC/AuNR/TiO_2 shows a large responsivity, whose peaks coincide with the UV−vis absorption spectrum (red). (f) Measured hydrogen production, measured photocurrent, and calculated photocurrent of the HER as a function of time. Reproduced with permission.[163] Copyright 2012, American Chemical Society. (g) Schematic of the cross-section of an individual photosynthetic unit, presenting the inner Au nanorod and TiO_2 cap decorated with platinum nanoparticles. (h) Corresponding TEM (left) and enlarged views of the platinum/TiO_2 cap (top right)

and Co-–OEC (bottom right). (i) Energy level diagram superimposed on the schematic of an individual unit of the plasmonic solar water splitter, showing the proposed processes in various parts. (j) Hydrogen evolution under visible-light illumination (λ > 410 nm) as a function of time. Experiments were conducted in a 6-h cycle. Illuminated area: 0.28 cm^2. Reproduced with permission. [170] Copyright 2013, Springer Nature.

In addition, plasmonic 1D nanostructures with longitudinal heterojunctions featuring multiple segments in the longitudinal direction were investigated. Wang *et al.* reported a programmable photocatalyst based on multi-segmented CdS–Au NRAs (nanorod arrays) with a sequential and highly tunable configuration, as shown in Figures 7 (a) and (b).[171] The absorption spectra in Figure 7 (c) indicate that the CdS–Au–CdS NRAs possess a relatively higher absorption in the entire visible region owing to the combined SPR effects of each Au nano-unit. Moreover, the SPR of the Au segments leads to enhanced EM fields, which can also increase the spatial separation distance of the photogenerated electron–hole pairs in the adjacent CdS segment, thereby effectively suppressing the recombination of the electron–hole pairs. Because the plasmonic resonance peak of the Au segment overlaps with the absorption of the CdS segment, the energy in localized plasmonic oscillations can be non-radiatively transferred from an Au segment to its adjacent CdS segment, leading to the generation of more electron–hole pairs in CdS. As presented in Figure 7 (d), the photocurrent is 3.94 mA/cm^2 for the CdS–Au–CdS nanorod arrays (NRAs) at 0 V (vs. Ag/AgCl), which is more than twice that of pure CdS nanowire arrays (NWAs) with a similar length. Figure 6 (e) depicts another impressive example proposed by Wang *et al.*, in which the nanobamboo array (NBAs) architecture of ZnS–Ag–CdS–Au–CdSe was fabricated.[172] Figures 7 (f) and (g) portray a clear decrease in photoluminescence upon the introduction of Au and Ag segments into the ZnS–CdS–CdSe NBAs. Further analysis reveals that the ZnS–Ag–CdS–Au–CdSe NBAs possess a shorter decay lifetime, indicating a faster interfacial electron transfer in the structure. The interfacial photo-induced charge transfer (PICT) processes in the ZnS–Ag–CdS–Au–CdSe nanobamboo are displayed in Figures 7 (h). These results demonstrate that the plasmonic metal segments interposed between semiconductor segments can acts as intermediate electron relays and channels, effectively prolonging the carrier lifetime while facilitating charge transport in the photoelectrode.

On a macroscopic level, longitudinal heterojunction 1D nanostructure arrays can be used as essential components in large-scale energy conversion devices. Owing to the devisable cooperation of the unique physical and chemical properties of each component, these smart architectures exhibit excellent synergistic performance in enhancing the solar-to-chemical energy conversion efficiency.

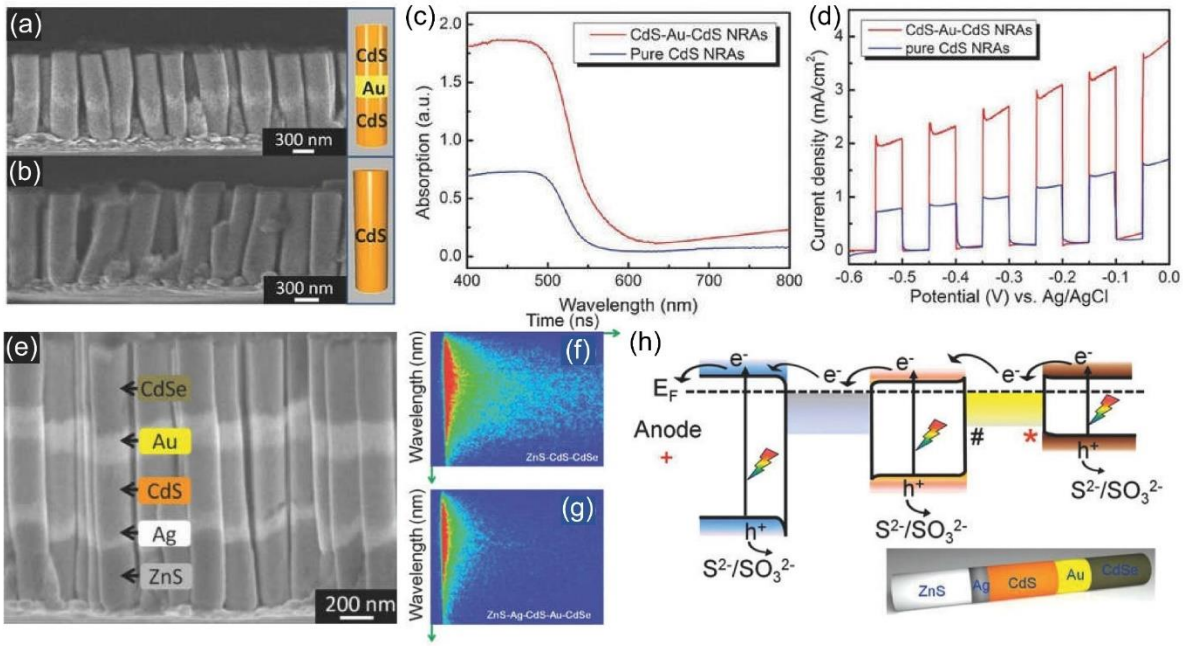

Figure 7. SEM images of (a) the side view of CdS–Au–CdS nanorod arrays (NRAs) and (b) pure CdS NRAs. (c) Absorption spectra of the pure CdS NRAs and the CdS–Au–CdS NRAs. (d) Linear sweep voltammogram curves of the pure CdS NRAs and CdS–Au–CdS NRAs in an aqueous solution of 0.2 M Na_2S/1 M Na_2SO_3 and potentials from −0.6 to 0 V (vs. Ag/AgCl), under the simulated AM 1.5 G illumination of 100 mW/cm^2. Reproduced with permission.[171] Copyright 2014, John Wiley & Sons, Inc. (e) SEM images of the side views of the ZnS–Ag–CdS–Au–CdSe nanobamboo arrays (NBAs). Photoluminescence images of (f) ZnS–CdS–CdSe NBAs and (g) ZnS–Ag–CdS–Au–CdSe NBAs obtained via a streak camera. The vertical axis is the wavelength (400–640 nm), and the horizontal axis denotes the time (≈90-ns window). (h) Schematic illustration of the interfacial photo-induced charge transfer (PICT) processes in the heterostructure of ZnS–Ag–CdS–Au–CdSe nanobamboo. Reproduced with permission.[172] Copyright 2015, John Wiley & Sons, Inc.

4.2.3 2D nanostructure arrays

In 2D nanostructure arrays, coupling properties are analyzed by varying the horizontal distance between adjacent individual nanostructures and combining them with semiconductors in different configurations. As presented in Figure 8 (a), an ordered plasmonic Au nanohole array was prepared through nanosphere lithography on an FTO substrate, followed by the growth of hematite nanorods inside the hole regions.[173] The absorption spectra in Figure 8 (b) indicates increased absorption over the entire spectral range for the hematite nanorods after combining with the Au nanohole array. By extracting the hematite background from the hematite/nanohole array sample, an absorption peak is manifested at approximately 650 nm. In particular, an intense local field gradient is crucial for enhancing the carrier lifetime in hematite. As revealed by the current density trends in Figure 8 (c), an enhancement factor as high as 10 is achieved by the hematite nanorod/gold nanohole array pattern with respect to that for bare hematite. The enhancement could be further quantified using mode-solver calculations for the hematite nanorods. Moreover, the waveguiding efficiency results in Figure 8 (d) reveal that the enhancement peak (425 nm) in the incident photon-to-electron efficiency (IPCE) spectrum is attributed to the SPPs, which launched a guided optical mode in the nanorod and increased light absorption at energies above the band edge of hematite. In contrast, the second enhancement peak in the IPCE is attributed to the PIRET effect at wavelengths below the band

edge of hematite. Consequently, photonic (13-time enhancement at 425 nm) and plasmonic energy-transfer enhancement (18-time enhancement at 650 nm) are achieved. Zhan *et al.* described a strategy based on the construction of a bare plasmonic bowtie array to quantitatively determine coupled photoelectronic (excited carriers) and photothermal effects.[174] The plasmonic electrode exhibited two typical plasmon resonances attributed to the LSPR of the bowtie and SPPs effect of the periodic array. Notably, the photocurrent enhancement produced by the Au nanoelectrode array was ~40 times higher than that of a smooth Au film.

Considering the structural configurations, forming core–shell metal-semiconductor nanostructures is a promising strategy for achieving a desirable plasmonic coupling effect.[157] To investigate the coupling effect in a size-controllable Au nanohole array (AuNHA), Zhang's group presented a nanocomposite Pt/TiO_2/AuNHA (refer to Figure 8 (e)).[140] In this nanocomposite, the Pt nanoparticles deposited onto the TiO_2 surface act as electron sinks, thereby enhancing the transfer efficiency of hot electrons. Figure 8 (f) displays the mechanisms of excitation and transfer of charge carriers in the Pt/TiO_2/AuNHA structure under visible light irradiation. Further analysis reveals that AuNHA excites both SPPs and LSPR modes in a single thin film, and the coupling effects of the two modes are improved by increasing the hole diameter during the same period. As presented in Figure 8 (g), the Pt/TiO_2/AuNHA samples show a notable enhancement within the wavelength range of 400−800 nm compared to that of the Pt/TiO_2/Au film. Particularly, the Pt/TiO_2/AuNHA(D90) sample exhibits a maximum efficiency of 0.5% at a peak of ~575 nm, which is 14.7 times that of the Pt/TiO_2/Au film. Another core–shell structure, based on Cu_2O/Cu half-shell (HS) arrays, exhibited excellent visible/NIR photocatalysis because of the efficient excitation of the LSPR effect of Cu and the combination of HEI, LEMF, and PIRET.[120] The reaction rates with Cu_2O/CuHS(224) were 84 times faster than those with the Cu_2O/Cu plate.

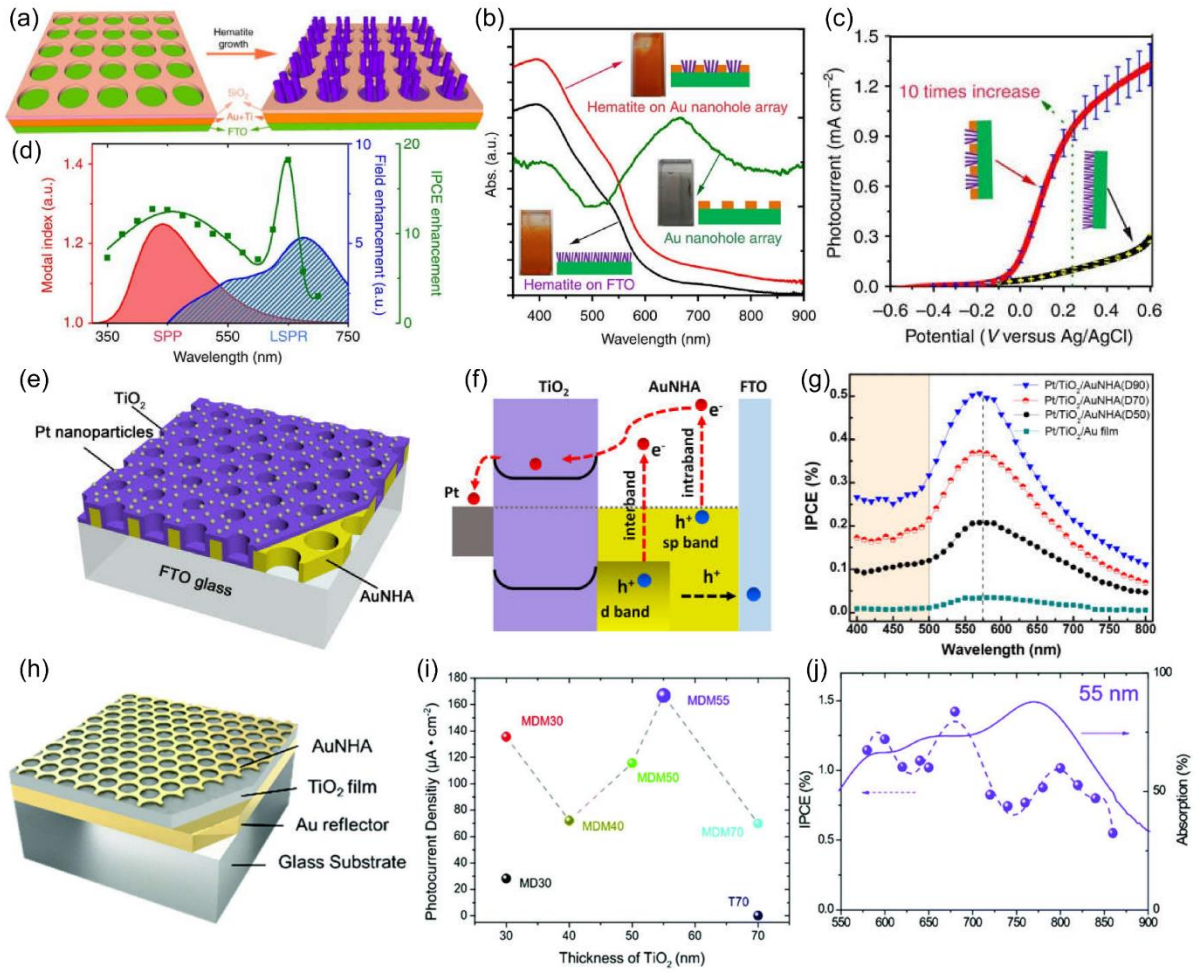

Figure 8 (a) Growth of the hematite nanorod array on the Au nanohole array. (b) UV–visible absorption spectra of the hematite nanorods and the Au nanohole array pattern. The insets show the pictures of photoanodes. (c) J–V curves under the illumination of AM 1.5 G full-spectrum solar light with a power density of 100 mW cm^{-2}. (d) Experimental IPCE characterized by the waveguiding efficiency and local field enhancement. Reproduced with permission.[173] Copyright 2013, John Wiley & Sons, Inc. (e) Layer structure of the Pt/TiO$_2$/AuNHA nanocomposite on the FTO glass. Considering a bottom-to-top configuration, this nanocomposite possesses an AuNHA layer (thickness: 60 nm), a TiO$_2$ thin film (thickness: 15 nm), and randomly dispersed Pt nanoparticles. (f) Energy band diagram of the Pt/TiO$_2$/AuNHA nanocomposite. (g) IPCE results as a function of wavelength for the Pt/TiO$_2$/AuNHA nanocomposites and control sample Pt/TiO$_2$/Au film. Reproduced with permission.[140] Copyright 2022, American Chemical Society. (h) Schematic of the AuNHA/TiO$_2$/Au metal–dielectric–metal (MDM) absorber. (i) Photocurrent density of the absorbers as a function of the TiO$_2$ thickness, in which 30, 40, 50, 55, and 70 nm represent the thicknesses of the TiO$_2$ film. T70 represents the structure of bare TiO$_2$ film with a thickness of 70 nm. (j) The IPCE spectra and absorption spectra of the MDM structures with the optimized TiO$_2$ thickness (55 nm). All the photocurrents and IPCEs were measured under the bias voltage of 0.5 V vs. SCE. Reproduced with permission.[116] Copyright 2021, Royal Society of Chemistry.

Another accessible approach involves adopting multi-interfacial plasmonic coupling using semiconductor photocatalysts as spacers to design a metal–dielectric–metal (MDM) structure.[175,176] Zhang's group proposed the use of multiple plasmonic resonant modes and strong horizontal/vertical coupling using a nanohole-based MDM nanocavity, as presented in Figure 8 (h).[116] Unlike common MDM structures, in addition to the F–P cavity mode in the dielectric layer, the top layer of AuNHA is unique—it excites the LSPR mode in the Au nanoholes and launches the gap surface plasmon polariton (GSPP) mode on the Au reflector

surface. Under the strong coupling condition, the energies of the three resonant modes can be exchanged coherently. As illustrated in Figures 8 (i) and (j), the spatial field overlapping of the three resonance modes enables strong mode coupling by optimizing the TiO_2 thickness to 55 nm, thereby leading to a notably enhanced average IPCE (~1.5%) and broadband photocurrent (170 $\mu A \cdot cm^{-2}$). Moreover, a similar structure was reported using the Au nanodisk array/hematite/Au film structure.[177] This approach yielded an approximately 2-fold increase over the hematite bandgap, resulting from the enhanced scattering and back reflection, and a 6-fold increase in the water oxidation photocurrent below the hematite bandgap, resulting from the plasmon decay of the gap-plasmon resonances in Au nanostructures and subsequent generation of hot carriers.

4.2.4 3D nanostructure arrays

To broaden the optical region of the plasmonic effects and the light-trapping region, 3D nanostructure arrays were considered to maximize their complementary absorption range. Isotropic configuration, achieved by completely coating metals with semiconductors, is an effective method for achieving optimized coupling effects between plasmonic metals and semiconductors. In this regard, Yang *et al.* reported an ultrathin hematite nanopillar array patterned on pre-synthesized Au nanopillars, as presented in Figure 9 (a).[93] As observed in the absorption spectra in Figure 9 (b), the Fe_2O_3 layer on the Au nanopillar arrays exhibits a large increase in the peaks at 624 and 681 nm with respect to those of the bare Fe_2O_3 film; this result is in good agreement matching with the measured IPCE enhancement spectrum. Additionally, the peaks at the same wavelengths coincide with the simulated absorption of Au nanopillars. Furthermore, the simulated electric-field maps, as displayed in Figure 9 (c), indicate that the plasmonic resonances at 624 and 681 nm exhibit characteristic evanescent field patterns near the Fe_2O_3–Au interfaces and light trapping at a non-resonant wavelength (451 nm), which synergistically yielded the enhancement in a broader spectral range. Similarly, Xu *et al.* fabricated an assembled CdS/Au pillar/truncated pyramid (PTP) photoanode by adopting a tunable three-dimensional Au PTP array as a plasmonic coupler, which exhibited a superior optical absorption of ~95% over a wide wavelength range.[94] Figures 9 (d) and (e) present the SEM images of the Au PTP array and CdS/Au PTP array coated with a 90-nm CdS film. As revealed by the measured spectrally resolved IPCE in Figure 9 (f), the CdS/Au PTP array shows a substantial IPCE enhancement over the wavelength range of 300−600 nm, compared with that of the CdS/Au plane and CdS/Au pillars. Further analyses of the simulated absorption and electric field distributions conclusively demonstrated that the significant IPCE enhancement is attributed to the SPR effects and photonic resonance modes in the Au PTPs, in which the SPR modes are dominant in the longer wavelength range of >450 nm and photonic modes contribute primarily to the shorter wavelength range of <450 nm. Furthermore, research based on antenna/spacer/reflector, such as moth-eye patterned Au/TiO_2 gap-plasmon structure[178] and Au/$BiVO_4$/WO_3/Au nanopatterned photoanodes[179], have reported extraordinary enhancement, which was attributed to the strong light–matter interaction from the photonic structure and the multiple resonance peaks from the randomly dispersed AuNPs. Furthermore, the strong EM field from the gap plasmon effect in the spacer, resulting from the coupling interaction between the reflector and antenna, facilitates charge separation and transport in the semiconductor.

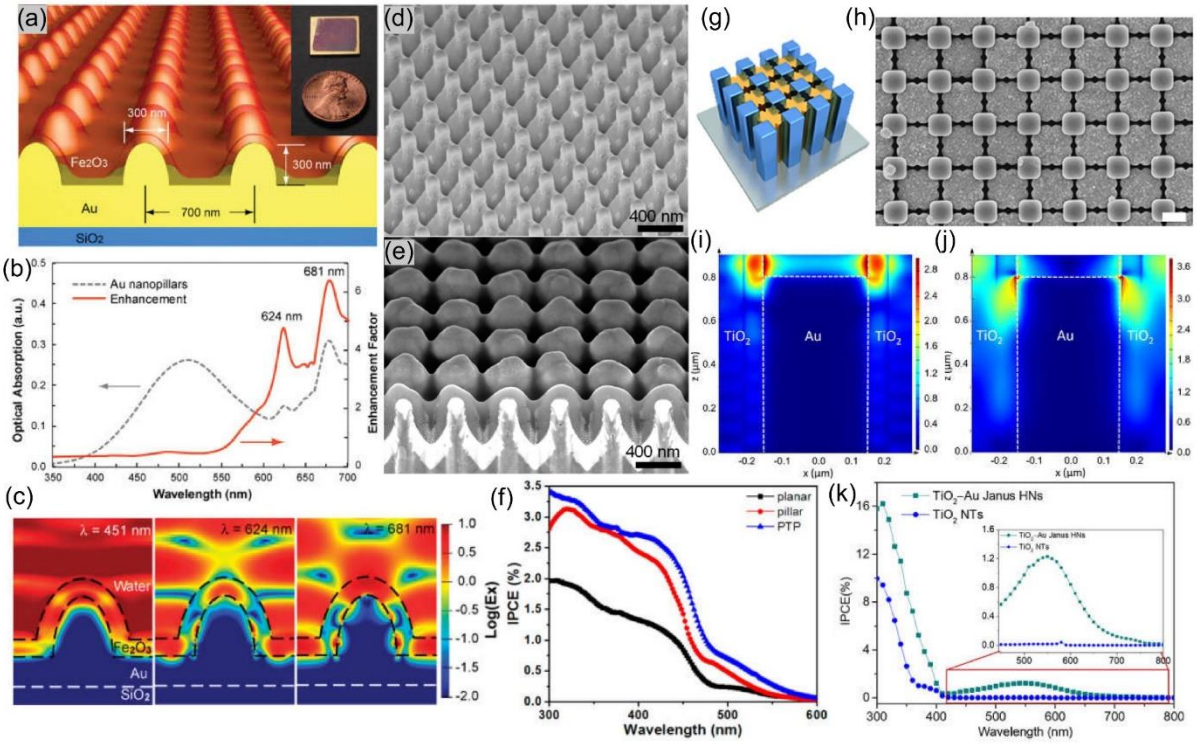

Figure 9. (a) Schematical diagram of the Au nanopillars. Inset: photograph of a 1.5 × 1.5 cm^2 sample uniformly patterned with Au nanopillars; a penny is also displayed to indicate the size. (b) Simulated optical absorption and (c) electric field-distribution maps of the Fe_2O_3 layer on the Au nanopillar arrays; these maps were obtained via the FDTD method. Reproduced with permission.[93] Copyright 2012, American Chemical Society. SEM images of (d) the Au PTP array and (e) CdS/Au PTP array coated with a 90-nm CdS film. (f) Simulated absorption spectra of the top (180 nm) and bottom (180 nm) sections of the Au PTPs and pillars. Reproduced with permission.[94] Copyright 2017, American Chemical Society. (g) Schematic diagram of Janus heteronanostructures (HNs). (h) SEM image of a typical TiO_2−Au Janus HNs. FDTD-simulated electric field ($|E/E_0|$) distributions for the TiO_2−Au Janus HNs at (i) 370 nm and (j) 540 nm. (k) IPCE spectra of the TiO_2–Au Janus HNs and TiO_2 nanotubes (NTs) over the wavelength range of 300−800 nm with no external bias. Reproduced with permission.[141] Copyright 2018, American Chemical Society.

Moreover, 3D nanostructure arrays with anisotropic configurations were investigated by partially integrating the metal and semiconductor structures at selected locations. The exposed domains of the metal and semiconductor facilitate charge-carrier transfer for redox reactions. Wen *et al.* developed an array of programmable Janus heteronanostructures (HNs) based on AAO binary pore templates.[141] A schematic diagram and SEM image of the TiO_2–Au Janus HNs are depicted in Figures 9 (g) and (h), respectively. In combination with the upgraded two-step anodization, the synthesis yielded high degrees of freedom for both nanocomponents of the Janus HNs, including morphologies, compositions, dimensions, and interfacial junctions. The finite-difference time-domain (FDTD) simulated electric-field distribution ($|E/E_0|$) at 370 nm in Figure 9 (i) reveals that an intensive electric field at the interface of the TiO_2–Au Janus HNs reached a large portion of the adjacent TiO_2-liquid interface, thereby inducing more hot carriers via the PIRET effect. In contrast, the strong $|E/E_0|$ distribution at 540 nm in Figure 9 (j) caused by the LSPR effect is mainly focused along the interface of the TiO_2 NTs–Au NRs below the top section of the Au NRs. To further elucidate the role of the Au NRs, the IPCE spectra in Figure 9 (k) is considered, revealing that the TiO_2–Au Janus HNs exhibit a

considerably higher and broader spectrum than those of TiO_2, and the observed photoconversion is dominated by the photoactivity of TiO_2 in the UV region. Furthermore, an IPCE spectrum is present in the visible region, with a peak of 1.21% at approximately 540 nm (inset of Figure 9k). Zhang *et al.* designed a novel photocathode based on a TiO_2/Au nanoring/Si nanohole (SiNH) heteronanostructure (HN).[129] The Au nanorings clinging to the sidewalls of the SiNH arrays not only induced a prominent enhancement of the light-harvesting ability but also excited vast hot electrons under light illumination. Coupled with the hotspots contributing to the HEI process, the maximum photon-to-energy conversion efficiency peaked at 13.3%.

These results validate that metallic 3D nanostructure arrays with isotropic or anisotropic configurations can not only improve the charge injection efficiency and optical path length but also enhance light absorption over a broad wavelength range. These features facilitate a controllable and scalable platform to tailor plasmonic and photonic resonances for efficient photocatalysis.

The material structures, based on plasmonic nanostructure arrays categorized from 0D to 3D, are summarized in Table 3. The relationships between the material structure and the corresponding photocatalytic performance, irradiation light, electrolyte, and reaction enhancement are examined herein.

Table 3. Nanostructure arrays-based materials for plasmonics enhancement in various photocatalytic reactions.

Category	Material structure	Photocatalytic reaction	Irradiation	Electrolyte	Enhancement performance	Ref.
0D	TiO_2-coated Au nanodots	Photocurrent density	Visible light (122.5 mW/cm^2)	0.1 M KOH	~ 25 times (vs. TiO_2)	[126]
	Nanoparticle arrays Ag@TiO_2	Photocurrent density	AM 1.5 light	1 M KOH	~ 40 times (vs. TiO_2)	[134]
	Nanoparticle arrays Ag@TiO_2	Photocurrent density	AM 1.5 light	0.1M Na_2SO_4	~ 38 times (vs. TiO_2)	[159]
	Au/TiO_2 hybrid NCAs	Hydrogen production	Visible light (150-W Xe lamp)	1:4 (v/v) methanol /aqueous solution	Up to 60% (vs. randomly distributed structure)	[112]
	Cu@Pt core–shell nanoparticle lattices	HER catalytic activity	White-light illumination	0.5 M Na_2SO_4	up to 60% (vs. dark condition)	[162]
	Au nanoparticle superlattices/CdS	Photocurrent density	AM 1.5 light	Na_2S/$Na_2S_2O_3$ (0.2 M/1 M)	~ 260% (vs. bare CdS film)	[161]
	Au@ZnO nanoparticle arrays	Photocurrent density	AM 1.5 G	0.35 M Na_2SO_3/0.25 M Na_2S	~ 12 times (vs. ZnO film) ~ 20 times (vs. Au nanoparticle array)	[160]
1D	Co–OEC/AuNR/TiO_2	Photocurrent density	Visible light	1 M potassium borate electrolyte	~ 20 times (vs. UV light)	[163]
	AuNR with top platinum/TiO_2 cap and side Co–OEC	Autonomous solar water-splitting	Visible light	1 M potassium borate electrolyte	-	[170]
	multi-segmented CdS–Au NRAs	Photocurrent density	AM 1.5 light	0.2 M Na_2S/1M Na_2SO_3	linearly increased by increasing the	[171]

					number of segments	
	ZnS–Ag–CdS–Au–CdSe NBAs	Photocurrent density	AM 1.5 light	0.2 M Na_2S/1 M Na_2SO_3	~ 2 times (vs. ZnS-CdS-CdSe NBAs)/ ~ 4 times (vs. ZnS-Au-CdS-Ag-CdSe NBAs)	[172]
2D	hematite nanorods–Au nanohole array	Photocurrent density	AM 1.5 light	1 M NaOH	~ 10 times (vs. pure hematite nanorods)	[173]
	AuNHA/TiO_2/Au MDM structure	Photocurrent density	Visible light (>490 nm)	2.5 mM $Fe_2(SO_4)_3$/10 mM $FeSO_4$/0.5 M Na_2SO_4	~ 1.26 times (vs. AuNHA/TiO_2 MD structure)	[116]
	Pt/TiO_2/AuNHA nanocomposite	Photocurrent density/ Degradation of MO	Visible light (>420 nm)	0.5 M Na_2SO_4/ 0.5 M Na_2SO_4/40 μM MO	~ 88.2 times (vs. Pt/TiO_2)/ ~ 9.4 times (vs. Pt/TiO_2/ Au film)	[140]
	Cu_2O/Cu half-shell arrays	Degradation of MO	Visible light (420− 1000 nm)	MO (1.2×10^{-2} mM)	~ 84 times (vs. Cu_2O/Cu plate)	[180]
	Au nanoelectrode array	Photocurrent density	Visible light (300 mW/cm^2)	0.2 M sodium sulfate aqueous solution	~ 40 times (vs. Au film)	[174]
	Au nanodisk arrays–hematite–Au film	Photocurrent density	Visible light (400− 600 nm/ > 600 nm)	1 M NaOH	~ 2 times / 6 times (vs. hematite–Au film)	[177]
3D	Fe_2O_3–Au nanopillars	Photocurrent density	AM 1.5 light	1 M NaOH	~ 50% (vs. Fe_2O_3-Au planar)	[93]
	CdS/Au PTP array	Photocurrent density	AM 1.5 light	Na_2S/ $Na_2S_2O_3$ (0.2 M/1 M)	~ 400% (vs. CdS/Au plane)	[94]
	TiO_2−Au Janus HNs	Photocurrent density/ Hydrogen production	AM 1.5 light	0.1 M NaOH or v/v 20% methanol mixed solution	~ 2.2 times (vs. TiO_2 NTs)/ ~ 4.6 times (vs. Pt/TiO_2 NTs)	[141]
	AuNP/TiO_2/Au moth-eye structure	Photocurrent density	Full-spectrum light/Visible light	0.5 M Na_2SO_4	~ 1.98 times/~ 15 times (vs. AuNP/TiO_2/Au film)	[178]
	Au/$BiVO_4$/Au nanostructure	Photocurrent density	AM 1.5 light	0.5 M Na_2SO_4	~ 3.23 (vs.bare $BiVO_4$)	[179]
	TiO_2/Au nanoring/SiNH	Photocurrent density	AM 1.5 light	0.5 M H_2SO_4	~ 2.4 times (vs. TiO_2/SiNH) [&]	[181]

[&] *Not published in the cited paper. Calculated by the authors of the present study.*

5. Conclusions and perspectives

In this overview, we discussed the fundamental plasmonic resonance and solar photocatalysis applications of plasmonic nanostructure arrays over a broad range from 0D to 3D. Moreover, the corresponding structural features, multiple resonance behavior, and ultrahigh local field

enhancement were extensively examined. Compared to isolated or disordered metal nanostructures, plasmonic nanostructure arrays exhibit unique advantages, including remarkably tunable absorption, enhanced local EM field, and extended hot-spot area over a wide spectral range. By characterizing the fundamental and optical properties for a better understanding of these aspects, the engineering of plasmonic nanostructure arrays will be accelerated for catering to technical needs and overcoming challenges, thereby emerging as a promising approach for practical applications.

However, the rational design of plasmonic nanostructure arrays for photocatalytic reactions remains hindered by certain challenges. These challenges are associated with the high cost of plasmonic materials. Studies on plasmonic nanostructure arrays have mainly focused on traditional plasmonic noble metals such as Au and Ag, which are unfavorable because of the high cost of raw materials. Recently, the use of other metals such as Cu, Ni, In, Fe, and Al, have emerged as cost-effective alternatives for sensing applications. The plasmonic nanostructure arrays in the reported studies operated predominantly in the visible and infrared (IR) regimes. To further extend the plasmonic response to UV and deep-UV regions, the use of Al, Cu, and other metals has drawn research interest owing to their large plasma frequency and strong local-field enhancement.[182,183] Reportedly, metal nitrides (ZrN and TiN),[184,185] titanium carbide, MXenes,[186] graphene, and highly doped semiconductors (Ta-doped TiO_2, Ga-doped ZnO, Al-doped ZnO, In-doped SnO_2)[187] can be used as alternatives to noble metals for visible-NIR responsive photocatalysis. As the SPR effects are closely associated with the material properties, new plasmonic materials will yield more degrees of freedom for nanostructure design.

The second challenge is the limited choice of functional semiconductor material. Studies report that semiconductors featuring a large bandgap generate a large open-circuit potential, and thus, a strong redox capacity, which is beneficial to a broad range of PEC reactions. In contrast, semiconductors with a small bandgap absorb a wide region of solar energy but offer weak redox capability. Manipulation of plasmonic nanostructure arrays with proper bandgap alignments of semiconductors is beneficial for solar energy harvesting, charge generation, separation, and transportation. Moreover, the physical parameters of metal nanostructure arrays, such as, work function, plasmonic band, and surface facet, and semiconductors, such as the position of the valance and conductive band, play a significant role in the plasmon-enhanced performance. In the non-radiative decay of plasmonic nanostructures, heat generation is associated with Ohmic losses, causing a temperature rise of tens to hundreds of degrees, depending on the incident power and plasmonic excitation.[188] Alternatively, in the relaxation process, hot charge carriers extracted from the plasmonic material can be injected into the semiconductor photocatalyst within 1 ps of plasmon generation to compete against electron–electron and electron–phonon scatterings. Thus, the integration and interface of semiconductors with plasmonic nanostructures are prerequisites for energy (or hot carrier) transfer between the two components. Tailoring the parameters of different materials, representing a highly systematic investigation, may trigger multiple plasmonic mechanisms

within the same device for broadband solar absorption, thereby yielding high performances.

Another notable challenge involves the analysis and simulation of plasmonic nanostructure arrays. Generally, numerical simulations of plasmonic nanostructure arrays feature an initial draft design of structures, and subsequently, the solution is derived in accordance with Maxwell's equations (such as FDTD simulation). Typically, several iterations of the design and simulation are involved. This approach is protracted and may not yield optimal results as it is constrained by numerous specific assumptions. In recent years, pioneering research on the structural design and performance prediction of plasmonic nanostructures has been conducted using artificial intelligence (AI) with deep learning.[189–192] After training thousands of synthetic experiments, the deep neural network can retrieve sub-wavelength dimensions solely based on far-field measurements, which can screen materials and structures and predict performance with acceptable accuracy.

Overall, the rational design of plasmonic nanostructure arrays is essential for yielding an optimal optical response, efficient charge transfer, and enhanced EM field. Considering their desirable advantages, plasmonic nanostructure hold promise for future applications, particularly in solar photocatalysis, biochemical sensing, and photodetection. We hope that this review of recent developments in plasmonic nanostructure arrays will propel the advancement of solar-energy conversion systems, which is essential for addressing global challenges such as energy crisis and environmental pollution and for facilitating sustainable practices.

Acknowledgments

This work was supported by the Research Grants Council (RGC) of Hong Kong (15221919, 15215620, and N_PolyU511/20) and The Hong Kong Polytechnic University (1-CD4V, G-SB4J, 1-YY5V, and 1-CD6U). It was also financially supported by the National Natural Science Foundation of China (61501316, 51505324, 62031022, and 62061160488), the Natural Science Foundation for Young Scientists of Shanxi Province, China (201801D221184), and the Central Guidance on Local Science and Technology Development Fund of Shanxi Province (YDZJSX2021A018).

Conflict of Interest

The authors declare no conflict of interest.

References

[1] X. Chen, L. Liu, P. Y. Yu, S. S. Mao, *Science (1979)* **2011**, *331*, 746.

[2] J. Liu, Y. Liu, N. Liu, Y. Han, X. Zhang, H. Huang, Y. Lifshitz, S. T. Lee, J. Zhong, Z. Kang, *Science (1979)* **2015**, *347*, 970.

[3] A. Fujishima, K. Honda, *Nature* **1972**, *238*, 38.

[4] H. Nishiyama, T. Yamada, M. Nakabayashi, Y. Maehara, M. Yamaguchi, Y. Kuromiya, H. Tokudome, S. Akiyama, T. Watanabe, R. Narushima, S. Okunaka, N. Shibata, T. Takata, T. Hisatomi, K. Domen, *Nature* **2021**, DOI 10.1038/s41586-021-03907-3.

[5] T. Takata, J. Jiang, Y. Sakata, M. Nakabayashi, N. Shibata, V. Nandal, K. Seki, T.

Hisatomi, K. Domen, *Nature* **2020**, *581*, 411.
[6] T. Hisatomi, K. Domen, *Nat Catal* **2019**, DOI 10.1038/s41929-019-0242-6.
[7] F. Cheng, G. Lin, X. Hu, S. Xi, K. Xie, *Nat Commun* **2019**, *10*, 1.
[8] Z. Z. Wang, D. Cao, R. Xu, S. Qu, Z. Z. Wang, Y. Lei, *Realizing Ordered Arrays of Nanostructures: A Versatile Platform for Converting and Storing Energy Efficiently*, **2016**.
[9] T. Hisatomi, J. Kubota, K. Domen, *Chem Soc Rev* **2014**, *43*, 7520.
[10] A. Bahramian, M. Rezaeivala, K. He, D. D. Dionysiou, *Catal Today* **2018**, 0.
[11] K. Appavoo, M. Liu, C. T. Black, M. Y. Sfeir, *Nano Lett* **2015**, *15*, 1076.
[12] G. Tagliabue, A. S. Jermyn, R. Sundararaman, A. J. Welch, J. S. DuChene, R. Pala, A. R. Davoyan, P. Narang, H. A. Atwater, *Nat Commun* **2018**, *9*, 3394.
[13] K. Appavoo, M. Liu, C. T. Black, M. Y. Sfeir, *Nano Lett* **2015**, *15*, 1076.
[14] H. bin Yang, J. Miao, S. F. Hung, F. Huo, H. M. Chen, B. Liu, *ACS Nano* **2014**, *8*, 10403.
[15] D. Li, J. Shi, C. Li, *Small* **2018**, *14*, 1.
[16] Q. Zeng, J. Bai, J. Li, B. Zhou, Y. Sun, *Nano Energy* **2017**, *41*, 225.
[17] X. Zhang, Y. L. Chen, R.-S. Liu, D. P. Tsai, *Reports on Progress in Physics* **2013**, *76*, 046401.
[18] M. M. Abouelela, G. Kawamura, A. Matsuda, *J Clean Prod* **2021**, *294*, 126200.
[19] Y. Wang, J. Zhang, W. Liang, H. Yang, T. Guan, B. Zhao, Y. Sun, L. Chi, L. Jiang, *CCS Chemistry* **2021**, 2127.
[20] Y. C. Chen, Y. K. Hsu, R. Popescu, D. Gerthsen, Y. G. Lin, C. Feldmann, *Nat Commun* **2018**, *9*, 1.
[21] G. Yu, J. Qian, P. Zhang, B. Zhang, W. Zhang, W. Yan, G. Liu, *Nat Commun* **2019**, *10*, 1.
[22] S. Linic, P. Christopher, D. B. Ingram, *Nat Mater* **2011**, *10*, 911.
[23] M. L. Brongersma, N. J. Halas, P. Nordlander, *Nat Nanotechnol* **2015**, *10*, 25.
[24] J. Li, S. K. Cushing, F. Meng, T. R. Senty, A. D. Bristow, N. Wu, *Nat Photonics* **2015**, *9*, 601.
[25] L. Zhang, N. Ding, L. Lou, K. Iwasaki, H. Wu, Y. Luo, D. Li, K. Nakata, A. Fujishima, Q. Meng, *Adv Funct Mater* **2019**, *29*, 1.
[26] N. Zhang, C. Han, X. Fu, Y.-J. Xu, *Chem* **2018**, *4*, 1832.
[27] T. G. U. Ghobadi, A. Ghobadi, E. Ozbay, F. Karadas, *ChemPhotoChem* **2018**, *2*, 161.
[28] R. Sellappan, M. G. Nielsen, F. González-Posada, P. C. K. Vesborg, I. Chorkendorff, D. Chakarov, *J Catal* **2013**, *307*, 214.
[29] G. H. Chan, J. Zhao, E. M. Hicks, G. C. Schatz, R. P. Van Duyne, *Nano Lett* **2007**, *7*, 1947.
[30] C. Lee, Y. Park, J. Y. Park, *RSC Adv* **2019**, *9*, 18371.
[31] N. Zhou, H. Zhu, S. Li, J. Yang, T. Zhao, Y. Li, Q. H. Xu, *Journal of Physical Chemistry C* **2018**, *122*, 7824.
[32] Y. Qu, R. Cheng, Q. Su, X. Duan, *J Am Chem Soc* **2011**, *133*, 16730.

[33] C. v. Hoang, K. Hayashi, Y. Ito, N. Gorai, G. Allison, X. Shi, Q. Sun, Z. Cheng, K. Ueno, K. Goda, H. Misawa, *Nat Commun* **2017**, *8*, 771.
[34] M. Tabatabaei, M. Najiminaini, K. Davieau, B. Kaminska, M. R. Singh, J. J. L. Carson, F. Lagugné-Labarthet, *ACS Photonics* **2015**, *2*, 752.
[35] B. Ai, Y. Yu, H. Möhwald, L. Wang, G. Zhang, *ACS Nano* **2014**, *8*, 1566.
[36] P. Wang, S. M. Zakeeruddin, J. E. Moser, M. K. Nazeeruddin, T. Sekiguchi, M. Grätzel, *Nat Mater* **2003**, *2*, 402.
[37] L. Wen, L. Liang, X. Yang, Z. Liu, B. Li, Q. Chen, *ACS Nano* **2019**, *13*, 6963.
[38] S. Kasani, K. Curtin, N. Wu, *Nanophotonics* **2019**, *8*, 2065.
[39] Z. Yuan, P. C. Wu, Y. C. Chen, *Laser Photon Rev* **2022**, *16*, 1.
[40] K. Yang, X. Yao, B. Liu, B. Ren, *Advanced Materials* **2021**, *33*, 1.
[41] H. Zhang, M. Zhou, H. Zhao, Y. Lei, *Nanotechnology* **2021**, *32*, DOI 10.1088/1361-6528/ac268b.
[42] L. Liang, Y. Xu, C. Wang, L. Wen, Y. Fang, Y. Mi, M. Zhou, H. Zhao, Y. Lei, *Energy Environ Sci* **2015**, *8*, 2954.
[43] Y. Xu, M. Zhou, L. Wen, C. Wang, H. Zhao, Y. Mi, L. Liang, Q. Fu, M. Wu, Y. Lei, *Chemistry of Materials* **2015**, *27*, 4274.
[44] Y. Wang, M. Zhang, Y. Lai, L. Chi, *Nano Today* **2018**, *22*, 36.
[45] J. Jiang, X. Wang, S. Li, F. Ding, N. Li, S. Meng, R. Li, J. Qi, Q. Liu, G. L. Liu, *Nanophotonics* **2018**, *7*, 1517.
[46] W. Wang, M. Ramezani, A. I. Väkeväinen, P. Törmä, J. G. Rivas, T. W. Odom, *Materials Today* **2018**, *21*, 303.
[47] W. Wei, F. Bai, H. Fan, *Angewandte Chemie - International Edition* **2019**, *58*, 11956.
[48] Z. Wang, D. Cao, R. Xu, S. Qu, Z. Wang, Y. Lei, *Realizing Ordered Arrays of Nanostructures: A Versatile Platform for Converting and Storing Energy Efficiently*, **2016**.
[49] H. Zhao, M. Zhou, L. Wen, Y. Lei, *Nano Energy* **2015**, *13*, 790.
[50] R. Xu, L. Du, D. Adekoya, G. Zhang, S. Zhang, S. Sun, Y. Lei, *Adv Energy Mater* **2021**, *11*, DOI 10.1002/aenm.202001537.
[51] M. Zhou, Y. Xu, Y. Lei, *Nano Today* **2018**, *20*, 33.
[52] L. Mascaretti, A. Dutta, Š. Kment, V. M. Shalaev, A. Boltasseva, R. Zbořil, A. Naldoni, *Advanced Materials* **2019**, *31*, 1805513.
[53] M. Wang, M. Ye, J. Iocozzia, C. Lin, Z. Lin, *Advanced Science* **2015**, *3*, DOI 10.1002/advs.201600024.
[54] W. Ye, R. Long, H. Huang, Y. Xiong, *J Mater Chem C Mater* **2017**, *5*, 1008.
[55] S. A. Maier, *Plasmonics: Fundamentals and Applications*, Springer US, New York, NY, **2007**.
[56] A. N. Koya, X. Zhu, N. Ohannesian, A. A. Yanik, A. Alabastri, R. Proietti Zaccaria, R. Krahne, W. C. Shih, D. Garoli, *ACS Nano* **2021**, *15*, 6038.
[57] S. A. Maier, *Plasmonics: Fundamentals and Applications*, Springer US, New York, NY,

2007.
[58] S. A. Maier, *Plasmonics: Fundamentals and Applications*, Springer, **2007**.
[59] M. Li, S. K. Cushing, N. Wu, *Analyst* **2015**, *140*, 386.
[60] C. F. Bohren, D. R. Huffman, *Absorption and Scattering of Light by Small Particles*, John Wiley & Sons, **2008**.
[61] J. R. Lakowicz, *Plasmonics* **2006**, *1*, 5.
[62] W. L. Barnes, A. Dereux, T. W. Ebbesen, *Nature* **2003**, *424*, 824.
[63] C. Ng, S. Dligatch, H. Amekura, T. J. Davis, D. E. Gómez, *Adv Opt Mater* **2015**, *3*, 1582.
[64] R. Hernandez, R. Juliano Martins, A. Agreda, M. Petit, J. C. Weeber, A. Bouhelier, B. Cluzel, O. Demichel, *ACS Photonics* **2019**, *6*, 1500.
[65] J. Zhang, L. Zhang, W. Xu, *J Phys D Appl Phys* **2012**, *45*, DOI 10.1088/0022-3727/45/11/113001.
[66] Z. Li, S. Butun, K. Aydin, *ACS Photonics* **2015**, *2*, 183.
[67] R. Ameling, H. Giessen, *Nano Lett* **2010**, *10*, 4394.
[68] K. Srinivasan, M. Borselli, O. Painter, A. Stintz, S. Krishna, *Opt Express* **2006**, *14*, 1094.
[69] X. Wu, Y. Wang, Q. Chen, Y.-C. Chen, X. Li, L. Tong, X. Fan, *Photonics Res* **2019**, *7*, 50.
[70] Y. Long, *Solar Energy Materials and Solar Cells* **2011**, *95*, 3400.
[71] L. Michaeli, H. Suchowski, T. Ellenbogen, *Laser Photon Rev* **2020**, *14*, 1.
[72] V. G. Kravets, A. v. Kabashin, W. L. Barnes, A. N. Grigorenko, *Chem Rev* **2018**, *118*, 5912.
[73] L. Lin, Y. Zheng, *Nanoscale* **2015**, *7*, 12205.
[74] W. Chen, S. Zhang, M. Kang, W. Liu, Z. Ou, Y. Li, Y. Zhang, Z. Guan, H. Xu, *Light Sci Appl* **2018**, *7*, DOI 10.1038/s41377-018-0056-3.
[75] G. M. Akselrod, J. Huang, T. B. Hoang, P. T. Bowen, L. Su, D. R. Smith, M. H. Mikkelsen, *Advanced Materials* **2015**, *27*, 8028.
[76] D. O. Sigle, L. Zhang, S. Ithurria, B. Dubertret, J. J. Baumberg, *Journal of Physical Chemistry Letters* **2015**, *6*, 1099.
[77] K. H. Su, Q. H. Wei, X. Zhang, J. J. Mock, D. R. Smith, S. Schultz, *Nano Lett* **2003**, *3*, 1087.
[78] J. Ye, F. Wen, H. Sobhani, J. B. Lassiter, P. van Dorpe, P. Nordlander, N. J. Halas, *Nano Lett* **2012**, *12*, 1660.
[79] N. Liu, T. Weiss, M. Mesch, L. Langguth, U. Eigenthaler, M. Hirscher, C. Sönnichsen, H. Giessen, *Nano Lett* **2010**, *10*, 1103.
[80] N. Verellen, P. van Dorpe, C. Huang, K. Lodewijks, G. A. E. Vandenbosch, L. Lagae, V. v. Moshchalkov, *Nano Lett* **2011**, *11*, 391.
[81] M. Hentschel, M. Saliba, R. Vogelgesang, H. Giessen, A. P. Alivisatos, N. Liu, *Nano Lett* **2010**, *10*, 2721.
[82] M. F. Limonov, M. v. Rybin, A. N. Poddubny, Y. S. Kivshar, *Nat Photonics* **2017**, *11*, 543.

[83] D. Bekele, Y. Yu, K. Yvind, J. Mork, *Laser Photon Rev* **2019**, *13*, 17.
[84] X. Zhang, N. Biekert, S. Choi, C. H. Naylor, C. De-Eknamkul, W. Huang, X. Zhang, X. Zheng, D. Wang, A. T. C. Johnson, E. Cubukcu, *Nano Lett* **2018**, *18*, 957.
[85] P. Fan, Z. Yu, S. Fan, M. L. Brongersma, *Nat Mater* **2014**, *13*, 471.
[86] T. A. Saleh, *Environ Technol Innov* **2020**, *20*, 101067.
[87] V. v. Pokropivny, V. v. Skorokhod, *Materials Science and Engineering C* **2007**, *27*, 990.
[88] R. D. Oliveira, A. Mouquinho, P. Centeno, M. Alexandre, S. Haque, R. Martins, E. Fortunato, H. Águas, M. J. Mendes, *Nanomaterials* **2021**, *11*, DOI 10.3390/nano11071665.
[89] J. Wang, G. Duan, Y. Li, G. Liu, W. Cai, *ACS Appl Mater Interfaces* **2014**, *6*, 9207.
[90] M. Toma, G. Loget, R. M. Corn, *Nano Lett* **2013**, *13*, 6164.
[91] D. K. Oh, T. Lee, B. Ko, T. Badloe, J. G. Ok, J. Rho, *Frontiers of Optoelectronics* **2021**, *14*, 229.
[92] H. Im, S. H. Lee, N. J. Wittenberg, T. W. Johnson, N. C. Lindquist, P. Nagpal, D. J. Norris, S. H. Oh, *ACS Nano* **2011**, *5*, 6244.
[93] H. Gao, C. Liu, H. E. Jeong, P. Yang, *ACS Nano* **2012**, *6*, 234.
[94] R. Xu, L. Wen, Z. Wang, H. Zhao, S. Xu, Y. Mi, Y. Xu, M. Sommerfeld, Y. Fang, Y. Lei, *ACS Nano* **2017**, *11*, 7382.
[95] Y. Han, H. Wang, L. Qiang, Y. Gao, Q. Li, J. Pang, H. Liu, L. Han, Y. Wu, Y. Zhang, *J Mater Sci* **2020**, *55*, 591.
[96] S. J. Park, H. Han, H. Rhu, S. Baik, W. Lee, *J Mater Chem C Mater* **2013**, *1*, 5330.
[97] G. Ali, M. Maqbool, *Nanoscale Res Lett* **2013**, *8*, 1.
[98] J. McPhillips, A. Murphy, M. P. Jonsson, W. R. Hendren, R. Atkinson, F. Höök, A. v. Zayats, R. J. Pollard, *ACS Nano* **2010**, *4*, 2210.
[99] M. D. Austin, H. Ge, W. Wu, M. Li, Z. Yu, D. Wasserman, S. A. Lyon, S. Y. Chou, *Appl Phys Lett* **2004**, *84*, 5299.
[100] K. J. Byeon, H. Leea, *EPJ Applied Physics* **2012**, *59*, 1.
[101] S. Y. Chou, P. R. Krauss, P. J. Renstrom, *Appl Phys Lett* **1995**, *67*, 3114.
[102] S. Y. Chou, P. R. Krauss, P. J. Renstrom, *Science (1979)* **1996**, *272*, 85.
[103] M. Colburn, S. C. Johnson, M. D. Stewart, S. Damle, T. C. Bailey, B. Choi, M. Wedlake, T. B. Michaelson, S. V Sreenivasan, J. G. Ekerdt, in *Emerging Lithographic Technologies III*, SPIE, **1999**, pp. 379–389.
[104] Z. Su, W. Zhou, *Advanced Materials* **2008**, *20*, 3663.
[105] U. Malinovskis, R. Poplausks, I. Apsite, R. Meija, J. Prikulis, F. Lombardi, D. Erts, *Journal of Physical Chemistry C* **2014**, *118*, 8685.
[106] Y. Li, G. Duan, G. Liu, W. Cai, *Chem Soc Rev* **2013**, *42*, 3614.
[107] W. Lee, R. Ji, U. Gösele, K. Nielsch, *Nat Mater* **2006**, *5*, 741.
[108] J. W. Elam, D. Routkevitch, P. P. Mardilovich, S. M. George, *Chemistry of Materials* **2003**, *15*, 3507.
[109] L. Wen, Z. Wang, Y. Mi, R. Xu, S. H. Yu, Y. Lei, *Small* **2015**, *11*, 3408.

[110] Z. Wang, D. Cao, R. Xu, S. Qu, Z. Wang, Y. Lei, *Nano Energy* **2016**, *19*, 328.
[111] A. v. Whitney, B. D. Myers, R. P. van Duyne, *Nano Lett* **2004**, *4*, 1507.
[112] B. H. Wu, W. T. Liu, T. Y. Chen, T. P. Perng, J. H. Huang, L. J. Chen, *Nano Energy* **2016**, *27*, 412.
[113] J. Chen, R. Xu, Z. Yan, C. Tang, Z. Chen, Z. Wang, *Opt Commun* **2013**, *307*, 73.
[114] S. H. Lee, K. C. Bantz, N. C. Lindquist, S. H. Oh, C. L. Haynes, *Langmuir* **2009**, *25*, 13685.
[115] T. Qiu, B. Luo, E. M. Akinoglu, J. Yun, I. R. Gentle, L. Wang, *Adv Funct Mater* **2020**, *30*, 2002556.
[116] Y. L. Wong, H. Jia, A. Jian, D. Lei, A. I. el Abed, X. Zhang, *Nanoscale* **2021**, *13*, 2792.
[117] X. Li, Y. Wu, L. Hang, D. Men, W. Cai, Y. Li, *J Mater Chem C Mater* **2015**, *3*, 51.
[118] W. Li, M. Khan, H. Li, L. Lin, S. Mao, J. M. Lin, *Chemical Communications* **2019**, *55*, 2166.
[119] K. Cho, G. Loget, R. M. Corn, *Journal of Physical Chemistry C* **2014**, *118*, 28993.
[120] K. Sugawa, N. Tsunenari, H. Takeda, S. Fujiwara, T. Akiyama, J. Honda, S. Igari, W. Inoue, K. Tokuda, N. Takeshima, Y. Watanuki, S. Tsukahara, K. Takase, T. Umegaki, Y. Kojima, N. Nishimiya, N. Fukuda, Y. Kusaka, H. Ushijima, J. Otsuki, *Langmuir* **2017**, *33*, 5685.
[121] P. Y. Chung, T. H. Lin, G. Schultz, C. Batich, P. Jiang, *Appl Phys Lett* **2010**, *96*, DOI 10.1063/1.3460273.
[122] P. Zheng, S. Kasani, N. Wu, *Nanoscale Horiz* **2019**, *4*, 495.
[123] F. Hua, Y. Sun, A. Gaur, M. A. Meitl, L. Bilhaut, L. Rotkina, J. Wang, P. Geil, M. Shim, J. A. Rogers, A. Shim, *Nano Lett* **2004**, *4*, 2467.
[124] S. M. Park, X. Liang, B. D. Harteneck, T. E. Pick, N. Hiroshiba, Y. Wu, B. A. Helms, D. L. Olynick, *ACS Nano* **2011**, *5*, 8523.
[125] J. Y. Woo, S. Jo, J. H. Oh, J. T. Kim, C. S. Han, *Appl Surf Sci* **2019**, *484*, 317.
[126] H. J. Kim, S. H. Lee, A. A. Upadhye, I. Ro, M. I. Tejedor-Tejedor, M. A. Anderson, W. B. Kim, G. W. Huber, *ACS Nano* **2014**, *8*, 10756.
[127] SI, *Adv Energy Mater* **2018**, *8*, 1.
[128] Y. Wang, L. Wu, T. I. Wong, M. Bauch, Q. Zhang, J. Zhang, X. Liu, X. Zhou, P. Bai, J. Dostalek, B. Liedberg, *Nanoscale* **2016**, *8*, 8008.
[129] L. Zhang, X. X. Chen, Z. Hao, X. X. Chen, Y. Li, Y. Cui, C. Yuan, H. Ge, *ACS Appl Nano Mater* **2019**, *2*, 3654.
[130] C. G. Kuo, C. C. Chen, *Mater Trans* **2009**, *50*, 1102.
[131] K. C. Popat, G. Mor, C. A. Grimes, T. A. Desai, *Langmuir* **2004**, *20*, 8035.
[132] M. Wu, L. Wen, Y. Lei, S. Ostendorp, K. Chen, G. Wilde, *Small* **2010**, *6*, 695.
[133] A. Sangar, A. Merlen, V. Chevallier, P. Torchio, S. Vedraine, L. Escoubas, L. Patrone, F. Flory, L. Patrone, G. Delafosse, E. Moyen, M. Hanbucken, *Solar Energy Materials and Solar Cells* **2013**, *117*, 657.
[134] Z. Zhan, R. Xu, Y. Mi, H. Zhao, Y. Lei, *ACS Nano* **2015**, *9*, 4583.

[135] Q. Ye, R. Y. Cao, X. Wang, X. Q. Zhai, T. T. Wang, Y. Xu, Y. He, M. Jia, X. Su, L. H. Bai, T. W. Peng, H. Wu, C. Liu, Y. Y. Bu, X. H. Ma, Y. Hao, J. P. Ao, *J Lumin* **2022**, *244*, DOI 10.1016/j.jlumin.2022.118740.
[136] S. Hui, J. Gao, X. Wu, Z. Li, Y. Zou, Y. Song, H. Cao, *J Phys D Appl Phys* **2016**, *49*, DOI 10.1088/0022-3727/49/25/25LT02.
[137] A. Ganapathi, P. Swaminathan, L. Neelakantan, *ACS Appl Nano Mater* **2019**, *2*, 5981.
[138] Y. Feng, K.-D. Kim, C. A. Nemitz, P. Kim, T. Pfadler, M. Gerigk, S. Polarz, J. A. Dorman, J. Weickert, L. Schmidt-Mende, *J Electrochem Soc* **2016**, *163*, D447.
[139] Z. Zuo, Y. Wen, S. Zhang, *Nanoscale* **2018**, *10*, 14039.
[140] H. Jia, Z. Li, B. Wang, G. Xing, Y. L. Wong, H. Ren, M. Li, K.-Y. Wong, D. Lei, L.-W. Wong, J. Zhao, W. Zhang, S. Sang, A. Jian, X. Zhang, *ACS Photonics* **2022**, *9*, 652.
[141] L. Wen, R. Xu, C. Cui, W. Tang, Y. Mi, X. Lu, Z. Zeng, S. L. Suib, P. X. Gao, Y. Lei, *Nano Lett* **2018**, *18*, 4914.
[142] C. Clavero, *Nat Photonics* **2014**, *8*, 95.
[143] K. Wu, W. E. Rodríguez-Córdoba, Y. Yang, T. Lian, *Nano Lett* **2013**, *13*, 5255.
[144] M. Kim, M. Lin, J. Son, H. Xu, J. M. Nam, *Adv Opt Mater* **2017**, *5*, 1.
[145] L. v. Besteiro, A. O. Govorov, *Journal of Physical Chemistry C* **2016**, *120*, 19329.
[146] L. Wen, Y. Chen, L. Liang, Q. Chen, *ACS Photonics* **2018**, *5*, 581.
[147] L. v. Besteiro, P. Yu, Z. Wang, A. W. Holleitner, G. v. Hartland, G. P. Wiederrecht, A. O. Govorov, *Nano Today* **2019**, *27*, 120.
[148] L. v. Besteiro, X. T. Kong, Z. Wang, G. Hartland, A. O. Govorov, *ACS Photonics* **2017**, *4*, 2759.
[149] L. Chang, L. v. Besteiro, J. Sun, E. Y. Santiago, S. K. Gray, Z. Wang, A. O. Govorov, *ACS Energy Lett* **2019**, *4*, 2552.
[150] Y. Zhu, H. Xu, P. Yu, Z. Wang, *Appl Phys Rev* **2021**, *8*, DOI 10.1063/5.0029050.
[151] E. Cortés, W. Xie, J. Cambiasso, A. S. Jermyn, R. Sundararaman, P. Narang, S. Schlücker, S. A. Maier, *Nat Commun* **2017**, *8*, 1.
[152] H. Zhang, A. O. Govorov, *Journal of Physical Chemistry C* **2014**, *118*, 7606.
[153] J. H. Lee, H. Y. Cho, H. K. Choi, J. Y. Lee, J. W. Choi, *Int J Mol Sci* **2018**, *19*, DOI 10.3390/ijms19072021.
[154] S. K. Ghosh, T. Pal, *Chem Rev* **2007**, *107*, 4797.
[155] I. Romero, J. Aizpurua, G. W. Bryant, F. J. García De Abajo, *Opt Express* **2006**, *14*, 9988.
[156] D. ten Bloemendal, P. Ghenuche, R. Quidant, I. G. Cormack, P. Loza-Alvarez, G. Badenes, *Plasmonics* **2006**, *1*, 41.
[157] D. Liu, C. Xue, *Advanced Materials* **2021**, *33*, 1.
[158] B. Lamprecht, G. Schider, R. T. Lechner, H. Ditlbacher, J. R. Krenn, A. Leitner, F. R. Aussenegg, *Phys Rev Lett* **2000**, *84*, 4721.
[159] Z. Zhan, F. Grote, Z. Wang, R. Xu, Y. Lei, *Adv Energy Mater* **2015**, *5*, 1.
[160] Y. Sun, B. Xu, Q. Shen, L. Hang, D. Men, T. Zhang, H. Li, C. Li, Y. Li, *ACS Appl Mater Interfaces* **2017**, *9*, 31897.

[161] R. Xu, L. Wen, Z. Wang, H. Zhao, G. Mu, Z. Zeng, M. Zhou, S. Bohm, H. Zhang, Y. Wu, E. Runge, Y. Lei, *Adv Funct Mater* **2020**, *30*, DOI 10.1002/adfm.202005170.
[162] S. Deng, B. Zhang, P. Choo, P. J. M. Smeets, T. W. Odom, *Nano Lett* **2021**, *21*, 1523.
[163] J. Lee, S. Mubeen, X. Ji, G. D. Stucky, M. Moskovits, *Nano Lett* **2012**, *12*, 5014.
[164] B. Nikoobakht, M. A. El-Sayed, *Chemistry of Materials* **2003**, *15*, 1957.
[165] O. Elbanna, S. Kim, M. Fujitsuka, T. Majima, *Nano Energy* **2017**, *35*, 1.
[166] J. Wang, S. Pan, M. Chen, D. A. Dixon, *Journal of Physical Chemistry C* **2013**, *117*, 22060.
[167] G. A. Wurtz, W. Dickson, D. O'Connor, R. Atkinson, W. Hendren, P. Evans, R. Pollard, A. v. Zayats, *Opt Express* **2008**, *16*, 7460.
[168] D. P. Lyvers, J. M. Moon, A. V. Kildishev, V. M. Shalaev, A. Wei, *ACS Nano* **2008**, *2*, 2569.
[169] R. Atkinson, W. R. Hendren, G. A. Wurtz, W. Dickson, A. v. Zayats, P. Evans, R. J. Pollard, *Phys Rev B Condens Matter Mater Phys* **2006**, *73*, 1.
[170] S. Mubeen, J. Lee, N. Singh, S. Krämer, G. D. Stucky, M. Moskovits, *Nat Nanotechnol* **2013**, *8*, 247.
[171] X. Wang, C. Liow, D. Qi, B. Zhu, W. R. Leow, H. Wang, C. Xue, X. Chen, S. Li, *Advanced Materials* **2014**, *26*, 3506.
[172] X. Wang, C. Liow, A. Bisht, X. Liu, T. C. Sum, X. Chen, S. Li, *Advanced Materials* **2015**, *27*, 2207.
[173] J. Li, S. K. Cushing, P. Zheng, F. Meng, D. Chu, N. Wu, *Nat Commun* **2013**, *4*, 2651.
[174] C. Zhan, B. W. Liu, Y. F. Huang, S. Hu, B. Ren, M. Moskovits, Z. Q. Tian, *Nat Commun* **2019**, *10*, 1.
[175] X. Shi, K. Ueno, T. Oshikiri, Q. Sun, K. Sasaki, H. Misawa, *Nat Nanotechnol* **2018**, *13*, 953.
[176] Y. Cao, T. Oshikiri, X. Shi, K. Ueno, J. Li, H. Misawa, *ChemNanoMat* **2019**, *5*, 1008.
[177] A. Dutta, A. Naldoni, F. Malara, A. O. Govorov, V. M. Shalaev, A. Boltasseva, *Faraday Discuss* **2019**, *214*, 283.
[178] J. Jun, H. Kim, H. J. Choi, T. W. Lee, S. Ju, J. M. Baik, H. Lee, *Solar Energy Materials and Solar Cells* **2019**, *201*, 110033.
[179] B. Chen, Z. Zhang, M. Baek, S. Kim, W. Kim, K. Yong, *Appl Catal B* **2018**, *237*, 763.
[180] K. Sugawa, N. Tsunenari, H. Takeda, S. Fujiwara, T. Akiyama, J. Honda, S. Igari, W. Inoue, K. Tokuda, N. Takeshima, Y. Watanuki, S. Tsukahara, K. Takase, T. Umegaki, Y. Kojima, N. Nishimiya, N. Fukuda, Y. Kusaka, H. Ushijima, J. Otsuki, *Langmuir* **2017**, *33*, 5685.
[181] L. Zhang, X. Chen, Z. Hao, X. Chen, Y. Li, Y. Cui, C. Yuan, H. Ge, *ACS Appl Nano Mater* **2019**, *2*, 3654.
[182] M. Lee, J. U. Kim, K. J. Lee, S. Ahn, Y. B. Shin, J. Shin, C. B. Park, *ACS Nano* **2015**, *9*, 6206.
[183] Z. L. Yang, Q. H. Li, B. Ren, Z. Q. Tian, *Chemical Communications* **2011**, *47*, 3909.

[184] U. Guler, S. Suslov, A. v. Kildishev, A. Boltasseva, V. M. Shalaev, *Nanophotonics* **2015**, *4*, 269.
[185] G. v. Naik, V. M. Shalaev, A. Boltasseva, *Advanced Materials* **2013**, *25*, 3264.
[186] K. Chaudhuri, M. Alhabeb, Z. Wang, V. M. Shalaev, Y. Gogotsi, A. Boltasseva, *ACS Photonics* **2018**, *5*, 1115.
[187] P. R. West, S. Ishii, G. v. Naik, N. K. Emani, V. M. Shalaev, A. Boltasseva, *Laser Photon Rev* **2010**, *4*, 795.
[188] Z. Chen, X. Shan, Y. Guan, S. Wang, J. J. Zhu, N. Tao, *ACS Nano* **2015**, *9*, 11574.
[189] Z. Liu, D. Zhu, K. T. Lee, A. S. Kim, L. Raju, W. Cai, *Advanced Materials* **2020**, *32*, 1.
[190] I. Malkiel, M. Mrejen, A. Nagler, U. Arieli, L. Wolf, H. Suchowski, *Light Sci Appl* **2018**, *7*, DOI 10.1038/s41377-018-0060-7.
[191] P. R. Wiecha, O. L. Muskens, *Nano Lett* **2020**, *20*, 329.
[192] P. R. Wiecha, A. Lecestre, N. Mallet, G. Larrieu, *Nat Nanotechnol* **2019**, *14*, 237.

Biographies of the authors

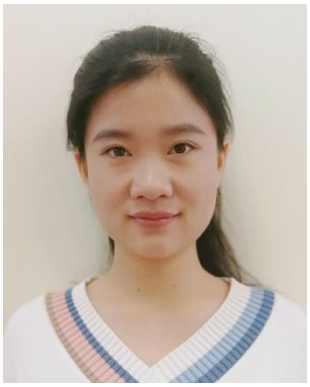

Huaping Jia received the B.Eng. degree in Communication Engineering from Taiyuan University of Technology in 2013. She is currently pursuing a Ph.D. degree in College of Computer and Information at Taiyuan University of Technology and is also a research assistant in the Department of Applied at Hong Kong Polytechnic University. Her research interests include the applications of the surface plasmonic effect in photocatalytic degradation, microfluidic reactors and water splitting.

Chi Chung Tsoi received his B.Sc. in Engineering Physics and M.Phil. from the Hong Kong Polytechnic University, Hong Kong, in 2015 and 2019. He is currently a PhD candidate at the Hong Kong Polytechnic University. His research interests are microfluidics and particle selection.

Dr. Abdel El Abed received his PhD in Physics at Paris Descartes university in 1992, where he was awarded later a permanent position as an Associate Professor (Maître de Conférences) at Paris Descartes University (now Paris Cité university). He obtained his Habilitation to Direct Research (HDR) in 2005 and moved, in 2013, to the Quantum and Molecular Photonics Laboratory at Ecole Normale Supérieure of Cachan and later (2019) to Light Matter and Interfaces Laboratory (Paris Saclay University). His recent research interests include droplet microfluidics, optofluidics, and photonics, with target applications in (bio)sensing, microthermometry, plasmonics, and photocatalysis.

Prof. Weixing Yu received his Ph.D. in Photonics from the Nanyang Technological University in 2005. He is currently at the Xi'an Institute of Optics and Precision Mechanics (XIOPM), Chinese Academy of Sciences. Before joining XIOMP in 2015, he worked at Shenzhen University for one year and at the Changchun Institute of Optics, Fine Mechanics and Physics (CIOPM), Chinese Academy of Sciences for five years, where he was promoted to full professor in 2009. His research interests include plasmonic optics, micro/nanooptics, bionic optical imaging, and novel spectral imaging technologies.

Prof. Aoqun Jian received the B.Eng. degree in electronic and information technology and M. Eng. degrees in microelectronics and solid electronics from the North University of China, Taiyuan, China in 2005 and 2008, respectively. He received the Ph.D. in the Department of Applied Physics from Hong Kong Polytechnic University in 2013. He is currently a professor at the College of Information at Taiyuan University of Technology. His current research interests include optical biosensors, particularly surface plasmon resonance, resonant optical tunneling effect, and optofluidics.

Prof. Shengbo Sang received the B.Eng. degree in communication engineering, and M Eng. degree in electronic science and technology from the North University of China in 2000 and 2006, respectively. He received the Ph.D. from the School of Mechanical Engineering, Ilmenau, Ilmenau University of Technology, Germany, in 2010. He is currently a professor at the College of Information at Taiyuan University of Technology. His current research interests include MEMS/NEMSs, optical devices, and biosensors.

Prof. Xuming Zhang is currently a full professor at the Department of Applied Physics, Hong Kong Polytechnic University, where he started as an assistant professor in 2009 and then became a tenured associate professor in 2015. He received BEng degree from the University of Science and Technology of China (USTC) in 1994, two M.Eng. degrees from the Shanghai Institute of Optics and Fine Mechanics (SIOM) in 1997, the National University of Singapore (NUS) in 2000, and a Ph.D. from Nanyang Technological University (NTU) in 2006. His current research interests include microfluidics, artificial photosynthesis, microoptics, nanophotonics, biomimetics, and green energy.